

Colours and luminosities of $z = 0.1$ simulated galaxies in the EAGLE simulations

James W. Trayford^{1*}, Tom Theuns¹, Richard G. Bower¹, Joop Schaye²,
Michelle Furlong¹, Matthieu Schaller¹, Carlos S. Frenk¹, Robert A. Crain³,
Claudio Dalla Vecchia^{4,5}, Ian G. McCarthy³

¹ *Institute for Computational Cosmology, Durham University, South Road, Durham, DH1 3LE*

² *Leiden Observatory, Leiden University, P.O. Box 9513, 2300 RA Leiden, the Netherlands*

³ *Astrophysics Research Institute, Liverpool John Moores University, 146 Brownlow Hill, Liverpool L3 5RF*

⁴ *Instituto de Astrofísica de Canarias, C/ Vía Láctea s/n, 38205 La Laguna, Tenerife, Spain*

⁵ *Departamento de Astrofísica, Universidad de La Laguna, Av. del Astrofísicisco Franciso Sánchez s/n, 38206 La Laguna, Tenerife, Spain*

Submitted 2015 April 15

ABSTRACT

We calculate the colours and luminosities of redshift $z = 0.1$ galaxies from the EAGLE simulation suite using the GALAXEV population synthesis models. We take into account obscuration by dust in birth clouds and diffuse ISM using a two-component screen model, following the prescription of Charlot and Fall. We compare models in which the dust optical depth is constant to models where it depends on gas metallicity, gas fraction and orientation. The colours of EAGLE galaxies for the more sophisticated models are in broad agreement with those of observed galaxies. In particular, EAGLE produces a red sequence of passive galaxies and a blue cloud of star forming galaxies, with approximately the correct fraction of galaxies in each population and with $g - r$ colours within 0.1 magnitudes of those observed. Luminosity functions from UV to NIR wavelengths differ from observations at a level comparable to systematic shifts resulting from a choice between Petrosian and Kron photometric apertures. Despite the generally good agreement there are clear discrepancies with observations. The blue cloud of EAGLE galaxies extends to somewhat higher luminosities than in the data, consistent with the modest underestimate of the passive fraction in massive EAGLE galaxies. There is also a moderate excess of bright blue galaxies compared to observations. The overall level of agreement with the observed colour distribution suggests that EAGLE galaxies at $z = 0.1$ have ages, metallicities and levels of obscuration that are comparable to those of observed galaxies.

Key words: galaxies: scaling relations, galaxies: simulation, galaxies: luminosity function, galaxies: colour-magnitude diagram

1 INTRODUCTION

The basic scenario for how galaxies form and evolve is well established: gas accretes onto deepening dark matter potential wells, cools and makes stars. Although this basic paradigm has been accepted for many years (e.g. Rees & Ostriker 1977; White & Rees 1978; White & Frenk 1991), many important aspects are still poorly understood. For example, the shape of the galaxy stellar mass function (GSMF) and of the halo dark matter mass function are quite different, so a simple formation model in which a halo of given mass con-

tains a galaxy whose stellar mass is equal to a fixed fraction of its halo mass is ruled out (e.g. White & Frenk 1991; Benson et al. 2003). In addition, galaxy surveys have revealed the presence of many correlations between the stellar properties of galaxies and galaxy mass, for example bimodality in the colour-magnitude diagram in the form of a blue cloud of star forming galaxies at lower mass, and a red sequence of mostly passive galaxies at higher mass (e.g. Baldry et al. 2004). Clearly, the dynamics and interaction physics of gas play important roles in determining the properties of galaxies.

It is thought that at the faint end of the GSMF supernovae (SNe) quench star formation in small galaxies (Larson

* E-mail: j.w.trayford@durham.ac.uk (JWT)

1974; Dekel & Silk 1986) with reionisation effectively preventing galaxies from forming in dark matter halos below a minimum mass (e.g. Rees 1986; Efstathiou 1992; Thoul & Weinberg 1995; Okamoto et al. 2008). Together these processes shape the GSMF at low stellar masses, with dark matter halos containing increasingly feeble galaxies with decreasing halo mass, until most halos remain dark (Sawala et al. 2014). In contrast, at higher galaxy masses it is thought to be the feedback from accreting black holes (BHs) that introduces a near exponential cut-off in the GSMF (Bower et al. 2006; Croton et al. 2006).

That feedback from star formation and BHs together shape the galaxy stellar mass function is energetically plausible, and semi-analytical models (e.g. Cole et al. 2000; Henriques et al. 2013; Gonzalez-Perez et al. 2014; Porter et al. 2014) and numerical simulations (e.g. Oppenheimer et al. 2010; Puchwein & Springel 2013; Vogelsberger et al. 2014; Schaye et al. 2015) that appeal to these processes are able to produce model GSMFs that compare well to observations at redshift $z \sim 0$. However, neither the semi-analytical models nor these simulations come anywhere near resolving the scales at which SNe and BHs inject energy, and so cannot *a priori* compute the net efficiency of the resulting feedback. Simulations therefore need to rely on a phenomenological description of these crucial processes occurring on unresolved (‘subgrid’) scales, using observations to calibrate the parameters that appear in the subgrid modules. It is then important to quantify the uniqueness and degeneracies in such modelling (Schaye et al. 2010; Crain et al. 2015), while at the same time use very high-resolution simulations (e.g. Hopkins et al. 2011; Creasey et al. 2013, 2015; Martizzi et al. 2014; Rosdahl et al. 2015) to try to bridge the gap between numerically unresolved and resolved scales.

The **E**volution and **A**ssembly of **Ga**Laxies and their **E**nvironment (EAGLE Schaye et al. 2015; Crain et al. 2015) suite of simulations uses the $z \sim 0.1$ GSMF, together with observations of galaxy sizes, to calibrate the subgrid physics modules. The GSMF is however not directly observable, but is inferred from luminosity functions after applying corrections for dust obscuration, and using simple stellar population (SSP) synthesis models that involve assumptions about stellar evolution, star formation histories, metallicity dependence of stellar emission, etc. With simulations such as EAGLE we can take the converse approach, attempting to reproduce the observational relations by inputting physical quantities tracked by the simulation. This has the advantage of allowing one to use properties modelled self-consistently such as gas content, metallicity and age to derive observable quantities, rather than treating them as free parameters in ‘SED fitting’ (e.g. Walcher et al. 2011) to estimate physical properties from observations. The colours of EAGLE galaxies are also an important test of the realism of the fiducial EAGLE model.

In this paper we examine to what extent mock luminosities computed from EAGLE galaxies using SSP models and a simple correction for dust obscuration reproduce the observed luminosity functions (in a range of broad bands), as well as galaxy colours. The aim is twofold: to provide a test of the realism of EAGLE, but also to test at some level whether the procedure of going from luminosity to stellar mass is reliable, as investigated in a recent paper by Torrey et al. (2014) using SED fitting of galaxies from the ILLUSTRIS

Table 1. Numerical parameters of those simulations of the EAGLE suite that are used in this paper. From left to right: simulation identifier, side length of cubic volume L in co-moving Mpc (cMpc), initial mass m_g of baryonic particles, Plummer-equivalent gravitational softening ϵ_{prop} at redshift $z = 0$ in proper kpc (pkpc).

Name	L cMpc	m_g M_\odot	$\epsilon_{\text{prop}}(z = 0)$ pkpc
Ref-L025N0376 (Ref-25)	25	1.81×10^6	0.70
Recal-L025N0752 (Recal-25)	25	2.26×10^5	0.35
Ref-L100N1504 (Ref-100)	100	1.81×10^6	0.70

simulation (Vogelsberger et al. 2014). It is perfectly possible that EAGLE galaxies have the wrong colours but the right stellar masses and stellar ages if errors in dust modelling are severe. However, if masses *and* colours agree with the data, then this increases our confidence that we can use EAGLE to investigate, for example, the origin of the observed bimodality of galaxy colours, or the nature of the galaxies that lie in between the red sequence and blue cloud in a colour-magnitude diagram.

In what follows we compare to photometric data from the *Galaxy And Mass Assembly* survey (GAMA Driver et al. 2011). This is a spectroscopic follow-up based on photometric data from the *Sloan Digital Sky Survey* (SDSS) and the *UK Infrared Digital Sky Survey* (UKIDSS), with details on the targeting and star-galaxy separation in Baldry et al. (2010) and on the GAMA-processed photometry, including matched aperture photometry from u to K in Hill et al. (2011). The GAMA survey has been designed for high uniform spectroscopic completeness (Robotham et al. 2010) and provides accurate redshifts (using AUTOz; Baldry et al. 2014) for a catalogue of $\sim 190,000$ galaxies, as presented by Taylor et al. (2014).

This paper is organised as follows. We begin with an overview of the EAGLE simulations, with emphasis on those aspects that are most relevant for the SSP modelling. In §3 we detail the development of our photometric model, concentrating on emission and absorption in §3.1 & §3.2 respectively. This model is applied to yield an optical colour-magnitude diagram (CMD) and multi-band luminosity functions (LFs) for galaxies, which are plotted and discussed in §4. We discuss our findings in §5 and summarise in §6.

2 THE EAGLE SIMULATIONS

Full details of the EAGLE simulations can be found in Schaye et al. (2015) and Crain et al. (2015) (hereafter S15 and C15 respectively); here we give only a brief overview. The EAGLE simulation comprises a suite of cosmological hydrodynamical simulations of periodic cubic volumes performed with the GADGET-3 TreeSPH code (which is an update of the GADGET-2 code last described by Springel 2005). Simulations were performed for a range of volumes and numerical resolutions. Here we concentrate on the reference model, using simulations at different resolution to quantify numerical convergence. The reference model assumes a Λ CDM cosmology with parameters derived from the ini-

tial *Planck* (Planck Collaboration et al. 2014) satellite data release ($\Omega_b = 0.0482$, $\Omega_{\text{dark}} = 0.2588$, $\Omega_\Lambda = 0.693$ and $h = 0.6777$, where $H_0 = 100 h \text{ km s}^{-1} \text{ Mpc}^{-1}$). Relevant properties are listed in Table 1.

We modified the treatment of hydrodynamics in GADGET-3 to use the conservative pressure-entropy SPH formulation of Hopkins (2013), the artificial viscosity switch introduced by Cullen & Dehnen (2010), an artificial conduction switch inspired by Price (2008), the C^2 kernel from Wendland (1995) and the timestep limiter of Durier & Dalla Vecchia (2012). Motivation and tests of this ‘ANARCHY’ version of SPH are presented in Dalla Vecchia (in preparation, see also Appendix A of S15), whereas Schaller et al (in preparation) examine the effects of using this modified version of SPH on galaxy properties.

A crucial aspect of EAGLE is that the parameters describing the subgrid modules have been calibrated on the observed $z \sim 0$ GSMF and galaxy sizes. This good agreement extends to many other observables that were not considered during the calibration, such as specific star formation rates (S15), the evolution of the GSMF (Furlong et al. 2014), molecular hydrogen fractions (Lagos et al. 2015), and absorption by intergalactic metals and neutral hydrogen (S15 Rahmati et al. 2015).

We now briefly describe those aspects of the subgrid model most relevant for this paper.

2.1 EAGLE Subgrid physics

The subgrid modules of EAGLE are partly inspired by the OWLS and GIMIC simulations (Schaye et al. 2010; Crain et al. 2009). Star formation is implemented as described in Schaye & Dalla Vecchia (2008): above the metallicity-dependent star formation threshold of Schaye (2004), cold enough particles ($T \sim 10^4 \text{K}$) are converted to star particles stochastically at a pressure-dependent rate that reproduces the observed Kennicutt-Schmidt star formation law. Each simulation star particle is assumed to represent a coeval population of stars formed with a Chabrier (2003) IMF, comprising stars with masses in the range $[0.1, 100] M_\odot$.

Stellar evolution is implemented as described in S15 and Wiersma et al. (2009a). We follow the production and release into the interstellar medium of 11 elements from three channels of stellar evolution (AGB stars, type I and type II SNe) using metallicity-dependent stellar lifetimes and stellar yields. We also track a separate ‘total’ metallicity (the mass fraction of elements more massive than helium), Z , to account for elements not tracked explicitly. When a gas particle is converted into a star particle it inherits the gas particle’s abundances. In addition to a particle metallicity, the simulation tracks smoothed metallicities which are computed using the SPH formalism to partly remedy the absence of mixing in the calculation (see Wiersma et al. 2009a for motivation). The ages, masses and metallicities of the star particles are the main ingredients of the simple stellar population (SSPs) models used below.

Radiative cooling and photo-heating in the presence of an optically thin UV/X-ray background, as computed by Haardt & Madau (2001), is accounted for as described in Wiersma et al. (2009b). The crucial processes of feedback from star formation is implemented by stochastically heating particles by a fixed temperature increment, as described and

motivated in Dalla Vecchia & Schaye (2012), and adapted for the simulation as described in S15 and C15. The formation of supermassive black holes and gas accretion onto them is implemented as in Booth & Schaye (2009), with modifications described in Rosas-Guevara et al. (2013) and S15, using a single feedback mode.

2.2 Identifying galaxies

To group star particles into ‘galaxies’, we proceed as follows. We begin by identifying dark matter halos using the friends-of-friends algorithm (Davis et al. 1985) with a linking length of 0.2 times the mean dark matter inter-particle spacing to identify regions that are overdense by a factor of ~ 200 (Lacey & Cole 1994). We then use the SUBFIND algorithm (Springel et al. 2001; Dolag et al. 2009) to identify self-bound substructures (subhalos) within halos of dark matter, stars and gas, which we identify with galaxies. Massive galaxies in EAGLE have extended density profiles. To assign luminosities to mock galaxies, we only include light emitted within a sphere of radius 30 proper kpc (pkpc), centred on the minimum of potential of each subhalo. The motivation for the choice of aperture is discussed further in section 3.1.4 and also in S15.

3 PHOTOMETRY

This section explains how we compute luminosities and colours for the simulated EAGLE galaxies. We begin by modelling luminosities of star particles, taking into account their ages and metallicities using population synthesis (section 3.1), the photometric system used to calculate magnitudes for direct comparison to observation (section 3.1.3), and the effects of dust absorption (section 3.2). The results of this section are summarised in Fig. 1, in which we plot histograms of $g - r$ colours of EAGLE galaxies in narrow stellar mass bins for different models, ranging from a simple emission model without dust, to a model including a multivariate treatment for dust.

3.1 Source Modelling

Below we compute luminosities of EAGLE galaxies from the ultraviolet (UV) to the near infrared (NIR). We limit ourselves to modelling stars, neglecting both nebular emission lines and light from AGN. Light absorbed by dust is assumed to be re-emitted in the far infrared which we do not study in this paper. As we also neglect scattering by dust, we treat individual wavelength bands independently. This approximation is supported by observations showing that scattering is a negligible contributor to the observed attenuation curve in galaxies (eg. Fischera et al. 2003).

Population synthesis models provide spectra for a discrete range of *simple stellar populations* (SSPs) (e.g. Bruzual & Charlot 2003; Maraston 2005; Leitherer et al. 1999). These SSPs represent populations of stars characterised by their total initial mass, formation time, and composition while assuming some stellar IMF. By decomposing the stellar component of a galaxy into a superposition of SSPs, the spectral energy distribution of an entire galaxy can be approximated.

We treat each EAGLE star particle as an SSP with given initial stellar mass, metallicity and age.

3.1.1 SSP Ingredients

Given our implementation of star formation, where gas particles are wholly converted into star particles, the typical mass of an EAGLE star particle is $\sim 10^6 M_\odot$. Stars are assumed to form with a Chabrier (2003) IMF (for consistency with the evolutionary models used in EAGLE), and they inherit the SPH-smoothed metallicity, Z , from their parent gas particle. The mass of a newly formed star particle is purely set by numerical resolution; the particle should not be thought of as representing a star cluster. In fact, $10^6 M_\odot$ is higher than the stellar mass formed in giant HII regions (e.g. Relaño & Kennicutt 2009; Zaragoza-Cardiel et al. 2014). This poor sampling of star formation can adversely affect luminosities of EAGLE galaxies. Indeed, a single recently formed star particle can affect the colour of a galaxy. We try to mitigate this numerical artifact by employing a finer sampling of the star formation history of recently formed stars, as described in Appendix A. We note that this has only a small effect for optical colours and thus for the results presented here.

The metallicity of stars affects their colours resulting in the well-known *age-metallicity* degeneracy (e.g. Worthey 1994). In addition, Z affects stellar evolution leading to differences between models, particularly for the AGB phase (e.g. Inoue 2012; Stancliffe & Jeffery 2007). In addition, metallicity of stars in EAGLE galaxies is set by the intricate interaction between enrichment of the ISM, gas accretion, and the extent to which galactic winds transport metals into the galaxy's circum- and intergalactic medium. The details of such metal mixing are still poorly understood and numerically challenging to model. Hence, there is no a priori guarantee that EAGLE yields realistic stellar metallicities.

The stellar mass - metallicity ($M_\star - Z_\star$) relations provide a useful way of characterising stellar abundances as a function of galaxy mass, and as shown in S15, the Ref-100 model yields stellar and gas-phase metallicities consistent with observations (Tremonti et al. 2004; Gallazzi et al. 2005; Zahid et al. 2014) for stellar masses $M_\star \gtrsim 10^{10} M_\odot$. However, lower-mass galaxies in EAGLE tend to be more metal-rich than observed, with numerical resolution playing a role: the higher-resolution Recal-25 simulation agrees with the data for $M_\star \lesssim 10^9 M_\odot$. It should also be noted that there are large systematics on the observed mass-metallicity relations (e.g. Kewley & Ellison 2008). We investigate the impact of stellar metallicity (Z_\star) on EAGLE colours in more detail in Appendix C. In our analysis, we use the EAGLE SPH-smoothed metallicities (Wiersma et al. 2009b) for each particle, which yield less noisy estimates of Z_\star .

3.1.2 Stellar Population Synthesis (SPS) Modelling

We adopt the GALAXEV population synthesis models of Bruzual & Charlot (2003), which provide the spectral energy distribution (SED) per unit initial stellar mass of a SSP for a discrete grid of ages (ranging from $t = 10^5$ to 2×10^{10} yr) and metallicities (ranging from $Z_\star = 10^{-4}$ to 0.05). We compute the SED for each stellar particle by interpolating the GALAXEV tracks logarithmically in age and

Z_\star , and multiplying by the initial stellar mass. Values of Z_\star in the simulation span a wider range than the models of Bruzual & Charlot (2003) encompass, and we extrapolate the model to predict colours for such extreme metallicities¹. We note that the more conservative approach of not extrapolating introduces a bias.

The GALAXEV spectra are based on stellar emission alone. These models are widely used, and have been shown to fit the local galaxy population in the optical bands with reasonable star formation and enrichment histories when used in conjunction with a dust model (e.g. Charlot & Fall 2000; Cole et al. 2000). The choice of population synthesis model has been shown to be largely unimportant for low-redshift galaxy populations, especially in optical bands (e.g. Gonzalez-Perez et al. 2014). The effect of different models (e.g. Maraston 2005; Conroy et al. 2009), and in particular the more uncertain impact of thermally-pulsing AGB stars (TP-AGB) on the SED, should however be considered when surveying higher redshift ($z \gtrsim 1$) galaxy populations (e.g. Maraston 2005; Gonzalez-Perez et al. 2014).

The Bruzual & Charlot (2003) models specify Z_\star values as absolute metal-mass fractions, where Z_\star affects the colours of stars through its impact on stellar structure and evolution - for example via the opacity, equation of state and mean molecular weight - and on stellar atmosphere models. Even so, the metallicity of the Sun (Z_\odot) *does* enter the population synthesis models because some parameters, such as the mixing length, are calibrated based on solar observables (Bressan et al. 1993). Recent literature determinations of Z_\odot have shown significant variability, with a minimum of $Z_\odot \sim 0.0126$ (e.g. Asplund et al. 2004) from the traditional value of $Z_\odot = 0.02$ assumed in Bruzual & Charlot (2003). Although the EAGLE simulations do not make use of any particular solar abundance pattern or Z_\odot value, a relatively low value of $Z_\odot = 0.0127$ (Allende Prieto et al. 2001) has been assumed in analysis for consistency with Wiersma et al. (2009b) (S15). The variation of Z_\odot generally results from a different determination of the abundance of some important element, such as O, N, C or Fe which also implies a variation of the abundance partition in the Solar model. In principle one should use GALAXEV SSP models with an abundance partition consistent with the assumed value of Z_\odot , and take into account effects arising from the different mixing length calibration, to compute colours self-consistently. For now we neglect any such changes and use the original GALAXEV SEDs, as the effects of this change on broad-band colours are expected to be small, as long as one makes use of the absolute value of the metallicity (Bressan 2014 *private comm.*)².

3.1.3 Photometric System

Given the SED for each star particle in the simulation, and a model for attenuation due to dust as a function of wavelength, we could compute the SED for each galaxy, and cal-

¹ We find that the effect of extrapolating metallicities, as opposed to clipping metallicities to that of the highest metallicity GALAXEV spectra, has a negligible effect on our results.

² We are grateful to S. Charlot and A. Bressan for their detailed explanation of the impact of Z_\odot on the GALAXEV model.

culate a broad-band magnitude by convolving with a broad-band filter. Here we use a much simpler method, namely we *first* convolve the GALAXEV spectra (for each value of age and metallicity) with broad-band filters to obtain ‘un-obscured’ broad-band luminosities. We use these to obtain a broad-band luminosity for an EAGLE galaxy. We only *then* take into account dust attenuation (as described below). If, as we assume, the wavelength dependence of the dust attenuation is not very strong (*i.e.* the optical depth does not vary strongly over the wavelength extent of the filter), then these two approaches yield very similar results. For the dust models discussed below, we verified that this is indeed the case (section 3.2).

We use the *ugrizYJHK* photometric system for optical and near infrared photometry, to enable a direct comparison to the GAMA survey (described in Driver et al. 2011; Hill et al. 2011). This survey is based on the photometry of SDSS (technical description in York et al. 2000) and UKIDSS, (technical description in Lawrence 2007). Note that when calculating photometry below, filter transmission curves include atmospheric absorption to enable a like-for-like comparison of simulation and observation. All magnitudes are calculated as rest-frame and absolute in the AB-system (Oke 1974) in which the apparent magnitude m_{AB} is defined as

$$m_{\text{AB}} \equiv -2.5 \log_{10}(F_{\nu}) - 48.6, \quad (1)$$

where F_{ν} is the isophotal flux density (in cgs units) in a particular band (e.g. Tokunaga & Vacca 2005).

3.1.4 Choice of aperture

Individual EAGLE ‘galaxies’ are identified as described in 2.2. We select galaxies with at least 100 star particles, whose stellar mass is reasonably well converged numerically (S15). The line of sight is chosen consistently to lie along an axis of our simulation coordinates, yielding an essentially randomised orientation for each galaxy.

Massive galaxies ($M_{\star} \gtrsim 10^{10.5} M_{\odot}$) in EAGLE have up to $\sim 40\%$ of their stellar mass in an extended halo beyond 30 pkpc of the galaxy centre (‘intra-cluster light’ since most of these massive galaxies are at the centre of a group or cluster). Observationally, such galaxies also tend to have extended light distributions and, unsurprisingly, the luminosity assigned to them depends on how such light is taken into account (e.g. Bernardi et al. 2013). We apply a constant aperture of 30 pkpc centred on the minimum of the gravitational potential of each subhalo for measuring the total luminosity, L , of a galaxy. The luminosity and colour of a galaxy with a significant intra-cluster light component do depend on whether we apply a 2D aperture or a 3D aperture. This change in colour is due to colour gradients but also due to the inclusion or exclusion of small blue satellite objects below the significance of those identified by SUBFIND. This is a similar issue to that encountered when isolating galaxies in astronomical data using software such as SEXTRACTOR (Jackson et al. 2010). We choose to apply a 3D spherical aperture, consistent with our previous analysis (S15, Furlong et al. (2014)). Such an aperture is shown in S15 to yield similar stellar masses to a Petrosian aperture, often used in observational studies.

The aperture definition is not standardised in observations, and can make a difference when a considerable frac-

tion of stellar material lies outside the aperture. This is illustrated for the Kron and Petrosian apertures in Driver (2012), where luminous galaxies with high Sérsic indices yield different magnitudes. Similarly, when analysing our simulations, the luminosities of EAGLE galaxies with $M_{\star} \gtrsim 10^{11} M_{\odot}$ are sensitive to the exact choice of aperture size. However, this is not the case for lower mass galaxies, for which the fraction of light in an extended halo is much lower.

3.1.5 Model N

The procedure for obtaining EAGLE galaxy photometry outlined above (sections 3.1.1-3.1.4) provides a model with no consideration of dust effects. This is hereafter referred to as model N. Model N provides a basis for comparison with photometry corrected for dust attenuation, as described below (sections 3.2.1-3.2.3). Panel a) of Fig. 1 shows the $g-r$ colour distribution of EAGLE galaxies for this model.

3.2 Dust model

We develop a simple *empirically calibrated* model for dust absorption, as opposed to a more physical modelling using ray-tracing, which we will present elsewhere. One advantage of such a model is that we can easily disentangle the effects of dust from those of the SPS modelling on galaxy colours. In addition, if we model dust attenuation using galaxy parameters that are provided by EAGLE but can also be inferred through observation, then we may calibrate the reddening of EAGLE galaxy colours empirically to reproduce observed trends. Keeping our dust model parametrisation independent of certain quantities, such as the gas distribution, also allows us more freedom to investigate the extent to which certain assumptions affect galaxy colours.

In our modelling, dust corrections are applied as a multiplicative factor that reduces a given broad-band luminosity. This factor is estimated at the effective wavelength of each filter (SDSS filter parameters taken from Doi et al. 2010, UKIRT filter parameters taken from Hewett et al. 2006), for a given dust prescription (neglecting changes in the dust opacity within a broad-band filter is a good approximation provided the dust model has a smooth wavelength dependence). In this way, dust obscuration depends on the subhalo properties of a galaxy alone, and we avoid handling entire SEDs and generating a new interpolation grid for each galaxy. This makes the analysis process very efficient. The approximation that reddening can be applied *after* the spectrum has already passed through a filter affects the $g-r$ optical colours by $\lesssim 0.02$ mag over the whole interpolation grid for the constant optical depth model discussed below.

3.2.1 Model GI: Galaxy-independent dust model

We begin by discussing the simplest dust model introduced by Charlot & Fall (2000), hereafter referred to as CF. This model includes two contributions to the dust optical depth in a galaxy ($\hat{\tau}_{\text{d}}$): (i) a transient component due to dust in stellar birth clouds ($\hat{\tau}_{\text{bc}}$), and (ii) a constant dust screen that represents dust in the ISM ($\hat{\tau}_{\text{ism}}$). The transmission T of this model is

$$T(\lambda, t') = \begin{cases} \exp\left(-[\hat{\tau}_{\text{bc}} + \hat{\tau}_{\text{ISM}}] \left(\frac{\lambda}{\lambda_v}\right)^{-0.7}\right) & , \text{ for } t' \leq t_{\text{disp}}, \\ \exp\left(-\hat{\tau}_{\text{ISM}} \left(\frac{\lambda}{\lambda_v}\right)^{-0.7}\right) & , \text{ for } t' > t_{\text{disp}}. \end{cases} \quad (2)$$

Here, t' is the stellar particle's age, t_{disp} is the dispersal time of the stellar birth cloud, λ is the wavelength of light, and $\hat{\tau}_{\text{ISM}}$ and $\hat{\tau}_{\text{bc}}$ characterise the total dust optical depth (due to ISM and birth-cloud, respectively), at wavelength λ_v . When a model SED of a galaxy is fit to an observed galaxy, $\hat{\tau}_{\text{ISM}}$ and $\hat{\tau}_{\text{bc}}$ can be used as fitting parameters to model dust (e.g. da Cunha et al. 2008). Alternatively, these parameters can be assigned constant values to model dust for a given population of galaxies as in Bruzual & Charlot (2003), but this does then not allow for variations between galaxies.

As a first approximation we simply take $\hat{\tau}_{\text{ISM}}$ and $\hat{\tau}_{\text{bc}}$ to be constants,

$$\begin{aligned} \hat{\tau}_{\text{bc}} &= 0.67 \\ \hat{\tau}_{\text{ISM}} &= 0.33, \end{aligned} \quad (3)$$

with $\lambda_v = 5500 \text{ \AA}$ and $t_{\text{disp}} = 10^7 \text{ yr}$, which were calibrated to fit starburst galaxies and were used for the recent analysis of the ILLUSTRIS simulations (Vogelsberger et al. 2014) by Genel et al. (2014) and Torrey et al. (2014). With the optical depths fixed, the colours of an EAGLE galaxy will only depend on the SSP modelling. Such an approximation was also used in the development of the GALAXEV model, where it was shown to work well when SED fitting a subset of the SDSS survey at $z = 0.1$ (Bruzual & Charlot 2003). The effect of this simple dust model on $g - r$ colours can be seen by comparing panels a and b in Fig. 1, and is discussed in more detail below.

In this simple model (model GI), the strength of the two screen components are fixed for each galaxy (and hence do not depend on e.g. its gas mass or metallicity) and are also independent of orientation. We discuss refinements of the dust model next.

3.2.2 Model GD: ISM-dependent dust model

To account for variations in metal enrichment in the interstellar medium (ISM) of galaxies, we use the mass-weighted SPH-smoothed metallicity (Wiersma et al. 2009b) calculated for star-forming gas in each EAGLE subhalo, Z_{SF} . This metallicity calculation is chosen to imitate observational measurement techniques (Tremonti et al. 2004; Zahid et al. 2014). As demonstrated in S15, the mass-metallicity relations in EAGLE are significantly affected by resolution, with the Recal-25 simulation showing better agreement with the observed $Z_g - M_*$ relation from Tremonti et al. (2004) than Ref-100 for $M_* \ll 10^{10} M_\odot$ ³. Near the knee of the mass function, however, the EAGLE mass-metallicity relation agrees well with observation (see S15).

³ Note, however, that the observed mass-metallicity relation suffers from calibration uncertainties that exceed the difference between Tremonti et al. (2004) and Ref-100 (Kewley & Ellison 2008) and that the more recent re-analysis by Zahid et al. (2014) falls in between Ref-100 and Tremonti et al. (2004) (see figure 13 of S15).

We take the analytic expression for the $M_* - Z_g$ mass-metallicity relation at $z = 0.1$ of Zahid et al. (2014), $Z_{\text{Z14}}(M_*)$, evaluated at the Milky Way stellar mass, $M_{\text{MW}} = 6.43 \times 10^{10} M_\odot$ (McMillan 2011), as the ISM metallicity represented by the optical depth values of Eq. (2). Assuming optical depth is proportional to metallicity, we then scale the optical depths $\hat{\tau}_{\text{bc}}$ and $\hat{\tau}_{\text{ISM}}$ that appear in Eq. (2) by the factor

$$\begin{aligned} \hat{\tau}_{\text{bc}} &\rightarrow \frac{Z_{\text{SF}}}{Z_{\text{Z14}}(M_* = M_{\text{MW}})} \hat{\tau}_{\text{bc}} \\ \hat{\tau}_{\text{ISM}} &\rightarrow \frac{Z_{\text{SF}}}{Z_{\text{Z14}}(M_* = M_{\text{MW}})} \hat{\tau}_{\text{ISM}}, \end{aligned} \quad (4)$$

for each EAGLE galaxy.

Making the dust optical depth depend on metallicity is physically well motivated, as it is indicative of the fraction of ISM mass in dust grains. Therefore, we must also take account of the gas mass to quantify how much dust is available for obscuration. We do so by making the dust optical depth dependent on the *cold gas* mass - but still neglect how that gas is distributed.

We approximate the cold gas mass, M_{ISM} , by the mass in star-forming gas, which in EAGLE means gas above a given metallicity-dependent density threshold and below a given temperature (see S15). We then scale the birth cloud and ISM dust optical depths by the ratio of M_{ISM} for the galaxy over the value for the Milky Way (which we take to be 10 per cent of M_* ; Mo et al. 2010; McMillan 2011). This scaling is derived from observations indicating that optical depths approximately scale with the overall gas surface density (Σ_g) of galaxies (e.g. Grootes et al. 2013; Boquien et al. 2013). By taking Σ_g as approximately $\propto M_{\text{ISM}}/R_*^2$, and since the $z = 0.1$ stellar mass-size relation is relatively flat for both EAGLE (S15) and observed galaxies (Shen et al. 2003), we approximate that $\tau \propto \Sigma_g \propto M_{\text{ISM}}$. Neglecting the R_*^{-2} dependence maintains a relatively simple parametrisation, and appears to have little effect on galaxy colours, due to the limited mass range over which reddening is significant.

Such a scaling has the desired effect of reddening gas-rich spiral galaxies more than gas-poor elliptical galaxies at the same M_* . The galaxy $g - r$ colour distributions for the model including metallicity and gas fraction dependent reddening (model GD) are shown in Fig. 1c. For comparison, we also show the $g - r$ colour distributions for EAGLE galaxies where the value of $Z_{\text{Z14}}(M_*)$ is used in Eq. (4), instead of Z_{SF} . Because low M_{ISM} values provide low optical depths for the stellar mass range where EAGLE and observed mass-metallicity relations differ ($M_* \ll 10^{10} M_\odot$), both treatments produce similar distributions.

3.2.3 Model GD+O: ISM-dependent dust model with orientation effects

Finally, we represent the dependence of obscuration on orientation with a simple toy model. We assume the dust geometry to be an oblate spheroid, with major to minor axial ratio of $q = a/b = 0.2$. This q value is commonly used to represent an axial ratio typical of the intrinsic stellar distribution in disc galaxies (e.g. Tully & Fisher 1977). We assign to each EAGLE galaxy an orientation $w = \cos(\theta)$, where θ is the angle between the galaxy's minor axis and the line of sight. To obtain a random orientation we randomly sample

w from a uniform distribution over the interval $[-1, 1]$. The line-of-sight depth through the dust spheroid is then

$$l(w) = a \frac{q}{\sqrt{q^2 + (1 - q^2)w^2}}. \quad (5)$$

We then scale $\hat{\tau}_{\text{ISM}}$ as

$$\hat{\tau}_{\text{ISM}} \rightarrow \frac{l(w)}{\langle l \rangle} \hat{\tau}_{\text{ISM}}, \quad (6)$$

so that the mean optical depth does not change. This scaling reduces the amount of dust obscuration for most galaxies by a small amount, yet increases τ by a factor ~ 2 for a small number of ‘edge-on’ systems. We assume a value of q that is appropriate for discs, but we note that elliptical galaxies - provided they have little cold gas - are not strongly reddened anyway, hence this orientation correction is not important for them. The $g - r$ colour histograms including orientation effects are shown as model GD+O in Figure 1d. We also show the colour distributions produced using more oblate geometries, with axial ratio values $q = 0.1$ and $q = 0.02$, for comparison.

4 RESULTS

In this section we examine the effects of dust modelling on the colours, luminosities, and colour-magnitude diagrams of EAGLE galaxies taken from the Ref-100 and Recal-25 models at redshift $z = 0.1$.

4.1 Galaxy colours as a function of stellar mass

We contrast $g - r$ colours for EAGLE galaxies in narrow (0.3 dex) bins of M_* for different models of dust absorption in Fig. 1 (panels a-d). In all panels, the blue line corresponds to the observed distribution from the GAMA survey (Taylor et al. 2014). Different panels show models with no dust (model N, panel a), a dust model that is independent of galaxy type (model GI, panel b), a model in which dust opacity depends on metallicity and gas fraction (model GD, panel c), and finally a model that in addition accounts for orientation effects (model GD+O, panel d). All models are shown as histograms, normalised to have unit integral. Models including dust are plotted as solid histograms, while the dashed histograms represent model N in all panels. Ref-100 distributions for the fiducial dust models are plotted in black, whereas Recal-25 distributions are plotted (for the lowest mass bin) in red. Model variations are also plotted for Ref-100, with a model using the observed mass-metallicity relation in panel c shown in green (see section 3.2.2) and models with alternative q values in panel d shown in green and yellow (see section 3.2.3).

The observed $g - r$ colours shift from very red massive galaxies (usually termed the ‘red sequence’), to a broader distribution in colours for $10^{9.8} \lesssim M_*/M_\odot \lesssim 10^{10.8}$, and finally a blue population (usually termed ‘blue cloud’) at lower stellar masses. There is little evidence for a strong ‘bimodality’ in observed colours even though the data is often interpreted that way. Such an interpretation is perhaps due to the bimodality seen at a fixed optical magnitude, where blue galaxies are pushed into higher luminosity bins.

Before comparing the models to the data, we investigate the effects of dust modelling, going from high- to low-mass galaxies (top to bottom rows in panels a-d). The most massive galaxies in the EAGLE Ref-100 simulation ($M_*/M_\odot \gtrsim 10^{11.2}$, top rows) have a relatively extended intrinsic colour distribution (model N). Including a model with dust reddening independent of galaxy properties incorrectly reddens the reddest galaxies even more (model GI) but taking into account the relatively low cold-gas masses of these galaxies returns the colours to close to their intrinsic values (model GD). The tail of bluer massive galaxies is significantly affected by dust, yielding a mono-modal distribution in the highest-mass bin. Including orientation effects (model GD+O) gives a slightly broader colour distribution for the fiducial axial ratio value of $q = 0.2$.

A similar trend is noticeable for galaxies in the second most massive bin ($10^{10.5} \lesssim M_*/M_\odot \lesssim 10^{11.2}$, second row from the top). Though the fiducial value of $q = 0.2$ for GD+O produces a similar distribution to GD in this bin, varying q values appears to have the strongest effect here. Smaller q values show a more pronounced bimodality, as the majority of galaxies are subject to less reddening, while a minority of ‘edge-on’ galaxies are heavily reddened to $g - r$ colours $\gtrsim 0.8$.

The third bin ($10^{9.8} \lesssim M_*/M_\odot \lesssim 10^{10.1}$, third row from the top) also behaves similarly: the intrinsically bluest galaxies get reddened slightly more than the intrinsically red galaxies with scatter due to orientation having a negligible effect.

Finally, the colour distribution for galaxies in the least massive bin ($10^{8.7} \lesssim M_*/M_\odot \lesssim 10^9$, bottom row) is also shown for the Recal-25 simulation. There is a large difference in colours between Ref-100 and Recal-25 for the least massive galaxies, which is predominately a resolution effect: at the resolution of Ref-100 the star formation rates in these low-mass galaxies is underestimated (S15) which makes the simulated galaxies too red. This striking resolution dependence is not surprising. In Ref-100, galaxies of mass $M_* \sim 10^9 M_\odot$ are represented by only $\sim 10^3$ star particles, and for a typical cold gas fraction of 10 per cent, by only 100 star-forming gas particles. We demonstrate in Appendix B that red and blue sequence colours for galaxies across the $10^{9.8} \lesssim M_*/M_\odot \lesssim 10^{10.1}$ range⁴ are quite similar in Ref-100 and Recal-25 - which gives us confidence that Recal-25 gives numerically converged answers for the bottom row of Fig. 1. However, the different environments probed by the Ref-100 and Recal-25 models also contribute to the difference in colours, in particular the strength of the red sequence, because the larger volume contains a population of satellite galaxies in massive halos. This is also shown in Appendix B and discussed further in section 5. Taking into account dust obscuration and orientation effects has little effect on the colours in Recal-25 for these low-mass galaxies, with model GD+O and N yielding nearly identical colour distributions.

We now turn to comparing the colours of EAGLE galaxies to the data, going from top (most massive) to bottom (least massive) bins in stellar mass and focusing on model

⁴ A larger mass range is used in Appendix B than in the third row of Fig. 1 so that Ref-25 and Recal-25 are sufficiently sampled.

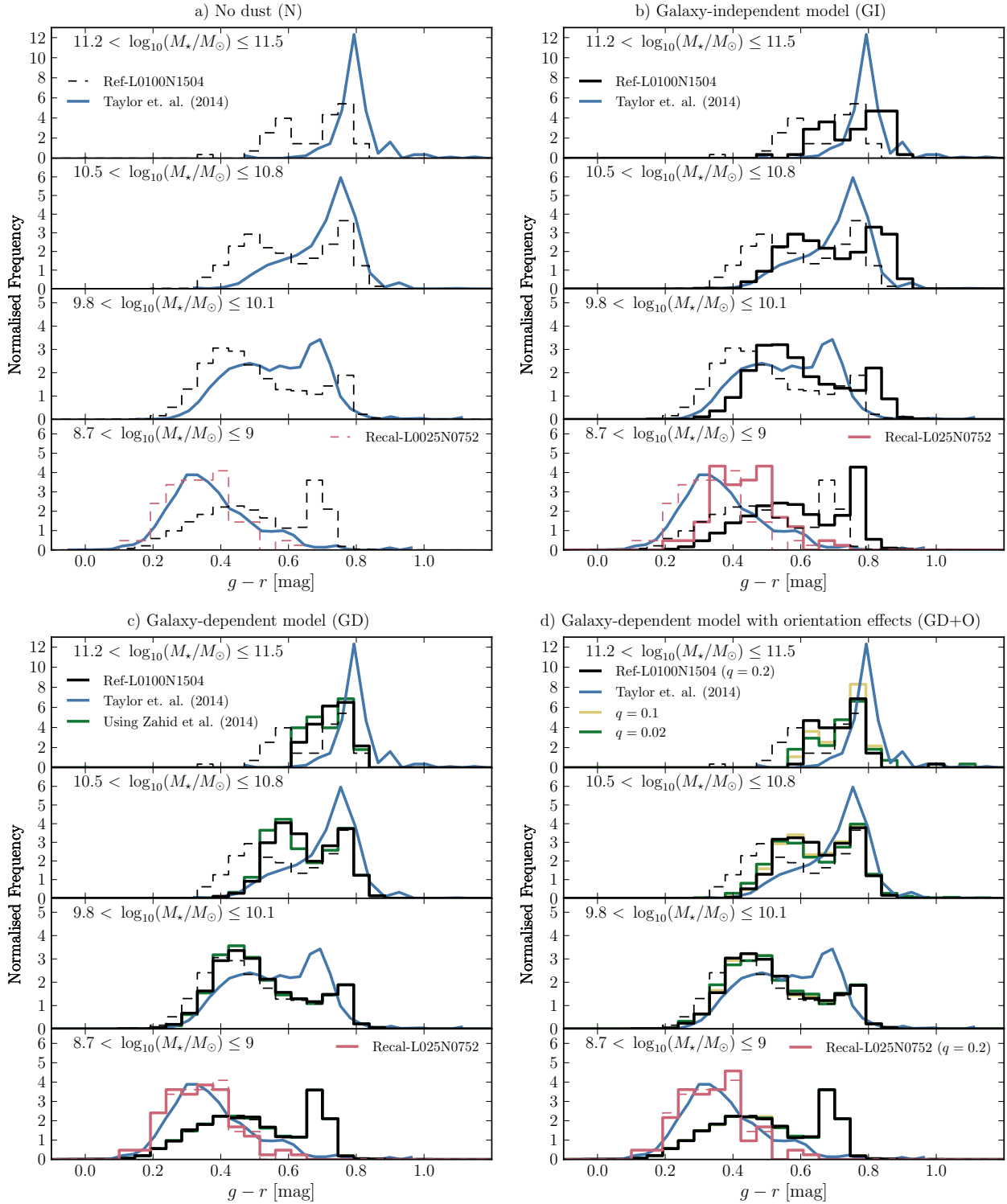


Figure 1. Rest-frame $g-r$ colour distributions for EAGLE galaxies at redshift $z = 0.1$, using 4 different models (panels a-d) for four non-contiguous ranges in stellar mass as indicated in the legend (top to bottom). Black lines indicate the fiducial Ref-100 galaxy population while red lines indicate the higher-resolution Recal-25 simulation. Dashed lines denote the unobscured SED (model N); these are repeated in each panel for comparison. Models shown are: model N without dust (panel a, see §3.1.5), model GI with galaxy independent dust (panel b, see §3.2.1), model GD where the dust obscuration depends on gas fraction and metallicity (panel c, §3.2.2), and model GD+O that in addition takes into account orientation effects (panel d, §3.2.3). Green and yellow lines show model variations in panels c and d (see sections 3.2.2–3.2.3 for details). Blue lines represent observed galaxy colours for the volume-limited sample of GAMA galaxies from Taylor et al. (2014). The figure shows the subtle quantitative effects that our different dust models have on the colour distributions of EAGLE galaxies in various M_* regimes, as is discussed further in the text.

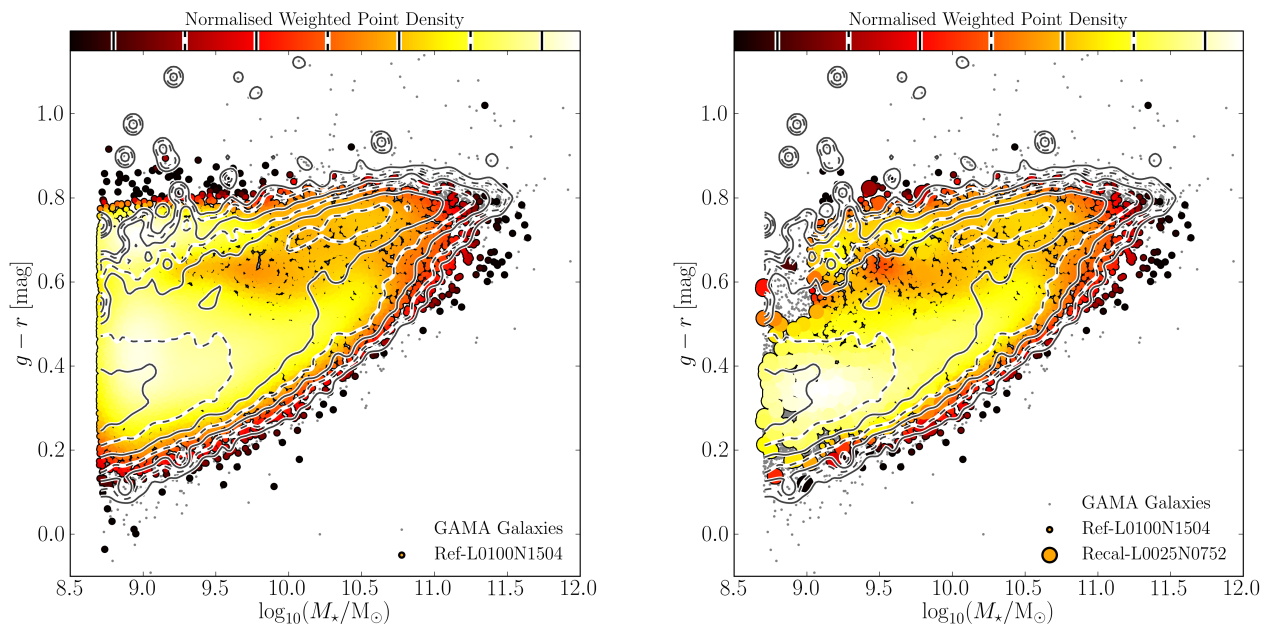


Figure 2. Rest-frame $g - r$ colour-stellar mass diagrams for EAGLE galaxies using photometry and dust reddening from model GD+O at $z = 0.1$ for simulation Ref-100 (*left panel*), and a composite set of EAGLE galaxies obtained by combining the higher-resolution model Recal-25 for galaxies with $M_* \lesssim 10^9 M_\odot$ and Ref-100 for $M_* > 10^9 M_\odot$ (*right panel*), cross-fading the sampling probability of the two galaxy populations linearly in $\log_{10}(M_*/M_\odot)$ (see text for details). Colours represent the point density of EAGLE galaxies of given M_* and $g - r$ colour (see text for details), with *black points* representing individual outlying EAGLE galaxies. Contours represent the colour- M_* distribution for a volume-limited set of GAMA galaxies from Taylor et al. (2014), with *grey points* representing individual outlying galaxies. The masses of observed galaxies are obtained through SED fitting, see Taylor et al. (2014). The colours are mapped to their equivalent contours in the colour bar. The colour bar covers 2 dex in point density with a contour spacing of 0.28 dex. A lack of numerical resolution makes lower-mass EAGLE galaxies too red in the left panel. The transition of colours of observed galaxies, from the red-sequence at stellar masses above $M_* \sim 10^{10.5} M_\odot$ to the blue cloud at lower stellar masses, is reproduced in the simulation, although the blue cloud extends to slightly higher M_* .

GD+O, Fig. 1d). At the massive end, the observed red sequence galaxies are about 0.05 mag redder in the data than in EAGLE. As the optical colours of old ($\gtrsim 10$ Gyr) stellar populations are dominated by metallicity effects (Bell & Rodgers 1969), this small colour difference is attributable to SSP metallicities. The $M_* - Z_*$ relation for EAGLE galaxies (S15) is seen to lie slightly below (by less than 0.1 dex) observational data in galaxies with $M_*/M_\odot > 10^{11}$, resulting in a slightly bluer red sequence colour. The data also has a tail to even redder colours not present in EAGLE. In contrast, the most massive EAGLE galaxies have a tail to *bluer* colours resulting from recent star formation. It could be that such star formation is shielded more effectively in the data (*i.e.* the value of $\hat{\tau}_{bc}$ used is too low), or alternatively that our AGN feedback scheme does not quite suppress star formation sufficiently. The higher than observed gas fractions for galaxy clusters in EAGLE (S15) could also contribute to the enhanced SFR of some simulated BCGs.

The red sequence of galaxies with $10^{10.5} \lesssim M_*/M_\odot \lesssim 10^{10.8}$ is very similar in the data and the simulation, but in EAGLE there are significantly more blue galaxies. The blue cloud starts to appear in the data for galaxies with $10^{9.8} \lesssim M_*/M_\odot \lesssim 10^{10.1}$, and its colour is very similar in EAGLE. However, in EAGLE the blue peak is stronger and the red peak occurs at a slightly redder colours ($g - r = 0.75$ compared to the observed value of 0.7). Using smaller values of q in GD+O does not improve agreement with observation

here. Dust reddening and orientation effects already play little role in setting the colours of EAGLE galaxies in this mass bin. Finally, in the lowest mass bin, $10^{8.7} \lesssim M_*/M_\odot \lesssim 10^9$, there is excellent agreement in the colour distributions of simulation and data and once more our dust reddening models are unimportant in setting EAGLE colours.

This level of agreement between galaxy colours in the simulation and the data is encouraging. By including metallicity and orientation effects in our dust treatment, we prevent the significant colour shift seen in the simple GI model. The validity of our dust model is discussed further in section 5. Despite the good agreement, there are some clear discrepancies between EAGLE and the GAMA colour distributions. These can be seen in the widths and relative strengths of red and blue populations. The latter discrepancy reflects the finding of S15 that the transition from actively star-forming to passive galaxies occurs at slightly (by a factor of ~ 2) too high mass in EAGLE.

The dependence of galaxy colours on stellar mass is further illustrated in Fig. 2, where the number density of galaxies in EAGLE with given rest-frame $g - r$ colour (computed using model GD+O) and stellar mass is compared to a volume-limited sample of GAMA galaxies taken from Taylor et al. (2014). Results are plotted down to stellar masses of $10^{8.7} M_\odot$, below which volume corrections due to the influence of line-of-sight structure become increasingly uncertain in the data (Taylor et al. 2014). The colour bar shows the

point density of EAGLE galaxies and how these map to the Taylor et al. (2014) contours.

The left panel shows the galaxies taken from simulation Ref-100. The simulation reproduces the trend seen in the data from galaxies being red above a stellar mass of $M_* \sim 10^{10.5} M_\odot$ to being predominantly blue below that. However, as also seen in the previous figure, there is a population of red ($g - r \sim 0.7$) low-mass ($M_* \sim 10^9 M_\odot$) galaxies in EAGLE that is not seen in the data. These galaxies are modelled using only ~ 1000 star particles; the right panel of Fig. 2 therefore uses the higher resolution simulation Recal-25 for galaxies below $10^9 M_\odot$ and Ref-100 above $10^9 M_\odot$, cross-fading one simulation into the other linearly in $\log(M_*)^5$. With this we aim to show the colour-mass distribution for a larger range of well-resolved galaxies ($\gtrsim 1000$ star particles), while avoiding a discontinuity that renders the overall distribution less clear.

Combining these two resolutions, the colours of EAGLE galaxies at given M_* track the data from the GAMA galaxies (Taylor et al. 2014) well. Both display a red sequence of massive galaxies which becomes redder with increasing stellar mass, and $g - r \sim 0.7$ at $M_* \sim 10^{10.5} M_\odot$. The simulation also reproduces the width of that sequence, albeit with a shallower slope. A blue cloud of galaxies appears both in EAGLE and GAMA below $M_* \sim 10^{10.5} M_\odot$, with $g - r \sim 0.45$ at $M_* = 10^{10.5} M_\odot$. At decreasing stellar mass, the location of the blue cloud becomes bluer, reaching $g - r \sim 0.35$ at $M_* = 10^9 M_\odot$. Overall we find that EAGLE reproduces the mean trends in galaxy colours well. Though the eradication of the faint red sequence in this sample is at least partly due to improved sampling, it also comes about because these galaxies are much less abundant in the higher resolution Recal-25 simulation (further discussion of the origin of this faint red population can be found in Section 5 and Appendix B).

In addition to the mean location of galaxy colours, there are outliers in both data and simulation. The GAMA data display a scatter to extremely red colours ($g - r > 1$) at all stellar masses only seen for one high-mass outlier in EAGLE. There is also a scattering of galaxies ~ 0.1 mag bluer than the main locus in GAMA that appear in EAGLE as well. Finally, EAGLE has some very massive, relatively blue galaxies ($M_* \sim 10^{11.5} M_\odot$, $g - r \sim 0.6$); although there are such galaxies in GAMA as well, they are more numerous in EAGLE, as is more easily seen in Fig. 1. We suggested before that these either imply too little dust reddening in star forming regions in EAGLE, or simply that some of these massive EAGLE galaxies are undergoing too much star formation despite the inclusion of AGN feedback.

⁵ The sampling frequency of Recal-25 galaxies in this plot are weighted a factor of 64 higher than Ref-100 galaxies to account for the smaller volume and a further factor of 2 lower to account for the boosted number counts in Recal-25 caused by poor sampling of large scale power in the smaller volume. This means that for masses $< 10^9 M_\odot$ each Recal-25 galaxy contributes a factor of 32 more to the point densities in Fig. 2 than a Ref-100 galaxy at mass $> 10^9 M_\odot$.

4.2 Luminosity functions and colour-magnitude diagram

Luminosity functions for model GD+O in rest-frame *ugrizYJHK* broad-band filters are plotted using absolute AB magnitudes in Fig. 3. The simulations Ref-100 and Recal-25 at redshift $z = 0.1$ are shown with Poisson error bars as solid black and red histograms respectively, becoming dashed when there are fewer than 10 galaxies per ~ 0.6 mag bin. For Recal-25 the bins are correlated, as can be seen for example in the *u*-band for bins $M - 5 \log(h) = -17.5$ to -18.5 , due to poor sampling of large-scale modes in the small volume. There is generally good agreement between the two runs, with Recal-25 typically less than a factor of two (0.3 dex) higher at the faint end, and by much less for the redder bands. Note that this higher-resolution simulation does not sample the exponential cut-off at high luminosities because of its small volume. Differences in resolution are most noticeable in bluer colours, particularly in *u*. As discussed before, in small galaxies the stellar feedback events driving outflows are poorly sampled and the star forming components are poorly resolved. As a result star formation rates and thus intrinsic colours are subject to considerable resolution effects. We see that the higher-resolution simulation yields higher star formation rates and hence bluer colours. We again note that this is not just a resolution issue: the Ref-100 volume contains a population of faint red quenched satellites of massive galaxies, which are simply not present in the much smaller Recal-25 volume, as discussed further in Appendix B. LFs in longer wavelength bands are consistent in shape between the two simulations (despite the small volume simulation being noisier).

Observed luminosity functions from Loveday et al. (2012) are plotted in each of the *ugriz* bands, which we fit with a single Schechter (1976) function,

$$\frac{1}{L_*} \frac{dn}{dL} = \phi_* \left(\frac{L}{L_*} \right)^\alpha \exp(-L/L_*) \frac{dL}{L_*}. \quad (7)$$

Single Schechter function fits are also taken from Driver (2012) and Jones et al. (2006). For the *ugriz* bands these are shown as grey shaded regions which are bounded by the fits to the observed luminosity function of Loveday et al. (2012) and Driver (2012), both based on data from GAMA. The differences between these observed luminosity functions result from the use of Kron and Petrosian magnitudes, respectively. The thickness of the grey band is thus a measure of how these different aperture choices affect the Schechter fit. For the *YJHK* band, we plot published Schechter fits, which are based on UKIDSS data.

There appears to be some discrepancy between Schechter fits from the observational papers and directly observed luminosity functions in the optical, as can be seen by comparing the Loveday et al. (2012) data with the Schechter fits. In particular, the data points appear systematically higher than the Schechter fit at the faint end and below the fit at the bright end. This is most visible in the *z*-band where the shaded region is narrowest. This could be a consequence of intermediate magnitude bins dominating the fit as this is where observational errors are minimal. It also shows that the single Schechter function is not a good fit to the observational data. In particular, it is unable to represent the observations at the faint end accurately (e.g. Loveday 1998).

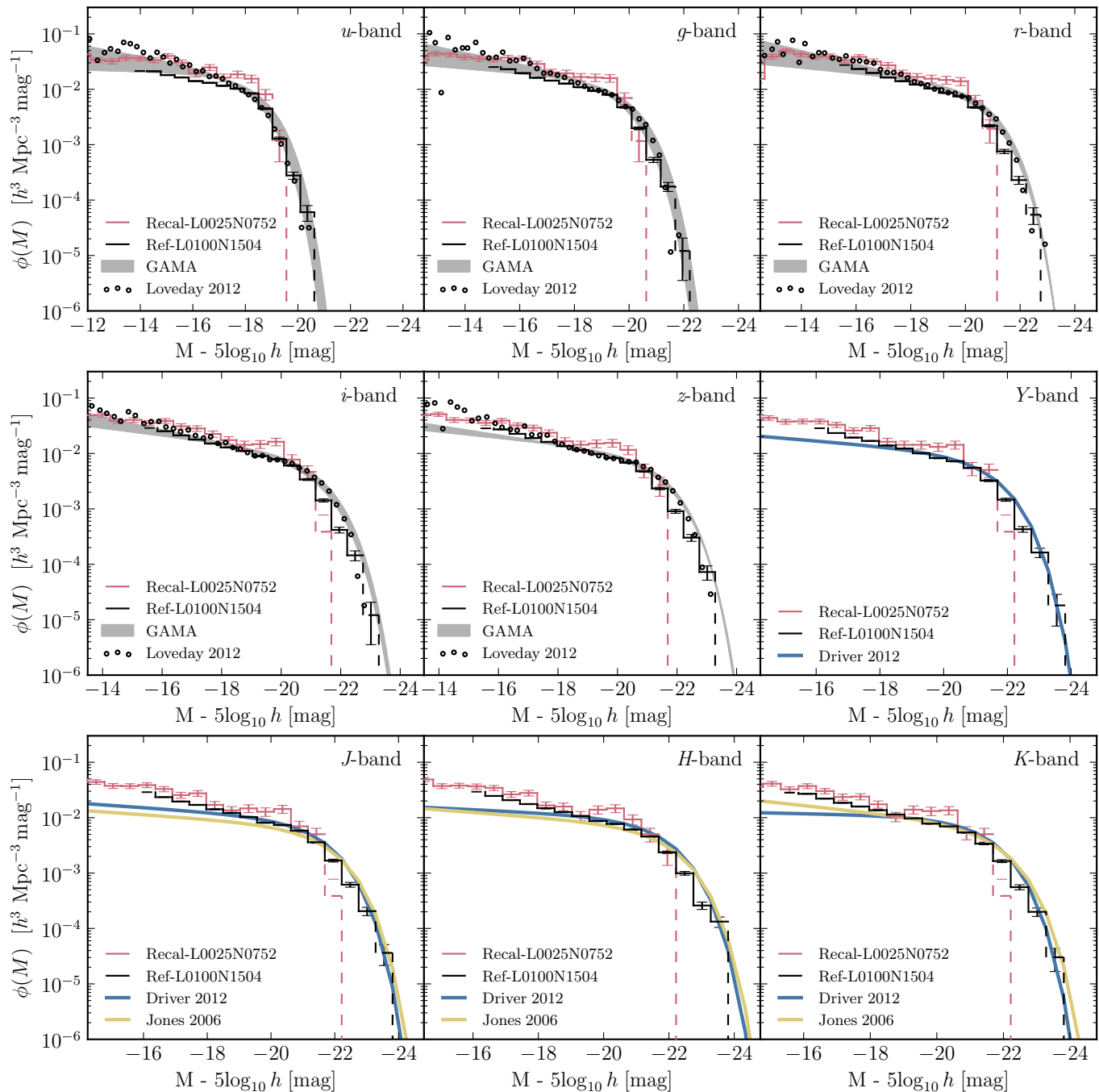


Figure 3. Luminosity functions in each band of the *ugrizYHJK* photometric system plotted for the fiducial 100 Mpc simulation (Ref-100) in black and the re-calibrated high resolution 25 Mpc simulation (Recal-25) in red, both at redshift $z = 0.1$, using the GD+O dust model. The Ref-100 function is plotted down to the faintest magnitude bin at which most galaxies are represented by >100 star particles. The simulation results from *ugriz* SDSS bands are compared to the Petrosian GAMA survey luminosity functions taken from Loveday et al. (2012), k -corrected to rest-frame magnitudes and plotted as empty circles. The region bound by the Schechter fits to the Driver (2012) and Loveday et al. (2012) luminosity functions is shaded in grey. As these two luminosity functions are measured using Kron and Petrosian magnitudes respectively, the grey area indicates the difference due to aperture definition. Schechter fits for UKIDSS band luminosity functions are taken from GAMA (Driver et. al. 2012) and from 6DF+2MASS (Jones et al. 2006) where available. All magnitudes are in the AB system. Error bars reflect Poisson errors with dashed lines indicating bins containing < 10 simulation galaxies. The EAGLE luminosity functions are similar to the observed fits across the spectral range, with some discrepancies discussed in Section 4.

Model	Description	r -band		
		$\phi_* [h^3 \text{ cMpc}^{-3}]$	α	$M_* - 5 \log_{10}(h) [\text{mag}]$
N	No dust	$7.0^{+0.7}_{-0.5} \times 10^{-3}$	$-1.26^{+0.02}_{-0.01}$	$-21.2^{+0.2}_{-0.2}$
GI	Galaxy-independent dust model	$7.6^{+1.0}_{-0.6} \times 10^{-3}$	$-1.23^{+0.04}_{-0.02}$	$-20.7^{+0.2}_{-0.1}$
GD	Z and M_{ISM} dependent	$8.2^{+1.0}_{-1.0} \times 10^{-3}$	$-1.23^{+0.05}_{-0.02}$	$-21.0^{+0.3}_{-0.3}$
GD+O	GD with orientation dependence	$8.3^{+1.3}_{-0.9} \times 10^{-3}$	$-1.23^{+0.04}_{-0.02}$	$-20.9^{+0.2}_{-0.2}$
Data	Loveday et al. (2012)	$9 \pm 0.7 \times 10^{-3}$	-1.26 ± 0.01	-20.7 ± 0.03

Table 2. Best-fitting Schechter function (Eq. 7) parameters for EAGLE AB-magnitude luminosity functions in the r -band for different dust models in simulation Ref-100 at redshift $z = 0.1$, and the observed luminosity function from Loveday et al. (2012). The EAGLE and observed luminosity functions are all fit over the magnitude range $-23.2 < r < -14.2$, 1σ errors on the best-fit parameters were computed using jackknife sampling.

The Driver (2012) and Jones et al. (2006) fits agree reasonably well, except for the faint-end slope in the K -band. The single Schechter fits are used here as simple indicators of the shape, position and normalisation of the observed luminosity functions, but clearly their exact location depends on details of how galaxies are identified in the data, and possibly on the range and assumed errors used in the fitting procedure. We compare the parameters of Schechter fits to EAGLE luminosity functions to observational fits in Table 2.

From Table 2 we see that the dust treatment has little effect on the shape of the r -band luminosity function. The effect of including dust using the GI model makes the knee position, M_* , 0.5 mag fainter magnitudes and increases the normalisation, ϕ_* . Scaling dust absorption by galaxy properties in GD serves to increase ϕ_* further, and makes M_* brighter by 0.3 mag. The GD and GD+O model luminosity functions provide Schechter fits that agree with the observational values within the errors. The faint-end slope, α , shows very little variation between all dust models, and all are consistent with the observational fit within the errors.

Comparing the GD+O EAGLE luminosity functions to the data in Fig. 2 shows a striking overall consistency from the UV to the NIR bands. The deviations are mostly of the same order as differences in fits to the published luminosity functions of different authors. The agreement is particularly good in the optical bands *ugriz*, where EAGLE tends to fall mostly inside the grey band that represents the dependence of the luminosity function on the choice of aperture. The excellent agreement over such a wide range of colours suggests that EAGLE forms the correct number of galaxies of a given stellar mass and that those galaxies have realistic star formation histories and metallicities.

Comparing blue bands ($u-g$) to redder bands ($J-K$) at the faint end, we notice that the EAGLE Ref-100 luminosity functions tend to be slightly low in blue bands relative to the data, but high in the red bands. This is a consequence of Ref-100 producing slightly too many low-mass galaxies (S15) which have too low star formation rates (Furlong et al. 2014). Resolution also plays a role: we plot galaxies with more than 100 star particles, where we know that the stellar feedback events generating outflows and star formation rates at the faint end are poorly resolved. In addition, even fainter galaxies with high star formation rates cannot scatter into the faint-end bins since we impose a cut in mass and not in magnitude.

The EAGLE luminosity function tends to drop below the observations at the ‘knee’ (L_*) in the Schechter function,

particularly in the bands red-ward of r . This is consistent with a slight underestimate in the masses of more massive EAGLE galaxies, as seen in the mass function plotted in S15.

The JHK bands also appear to have generally somewhat steeper faint-end slopes (parameter α in Eq.7) in EAGLE than the Schechter fits to the data. However, the data itself also shows a upturn at the faint end relative to the observed Schechter fits (circles in Fig. 3, see also Driver 2012). Generally, the single Schechter function fit tends to underestimate the luminosity function at the faint end (Loveday 1998). This is more pronounced in the JHK bands where the NIR sky is relatively bright (e.g. Sivanandam et al. 2012), leading to large uncertainties in the faint end data.

4.3 The $g-r$ colour-magnitude diagram

The colour-magnitude diagram of model GD+O for EAGLE is plotted in Fig. 4. As in the right panel of Fig. 2, we combined faint galaxies from the higher-resolution simulation Recal-25 for galaxies with $M_* < 10^9 M_\odot$ with galaxies from simulation Ref-100 at higher masses. As before, colours represent the number density of EAGLE galaxies in this plane, whereas contours show the corresponding data from the volume-limited catalogue of GAMA taken from Taylor et al. (2014). For both simulation and data, we only show galaxies with stellar mass $M_* > 10^{8.7} M_\odot$.

Fig. 4 now contains only ‘observable’ quantities for GAMA galaxies⁶, and in particular does not require any SED fitting. The overall agreement between EAGLE and the data is very good: the location and slope of the red-sequence is in good agreement, the transition to the blue cloud at $M_r - 5 \log(h) \sim 20$ is reproduced, and the blue $g-r \sim 0.3$ colours of the fainter blue galaxies are also reproduced. At the imposed mass cut of $M_* > 10^{8.7} M_\odot$, the colours and magnitudes of EAGLE galaxies agree well with the data. The bright blue galaxies that appear in EAGLE become slightly more discrepant with the data in this plot than in Fig. 2, due to the fact that bluer galaxies generally possess brighter r -band magnitudes for the same M_* .

The level of agreement between simulation and data in the colour-magnitude diagram shown in Fig. 4 is remarkable and suggests that these EAGLE simulations provide a

⁶ In practice the diagram still depends to a small extent on the applied cut in stellar mass at the faint end and on the choice of aperture to measure magnitudes.

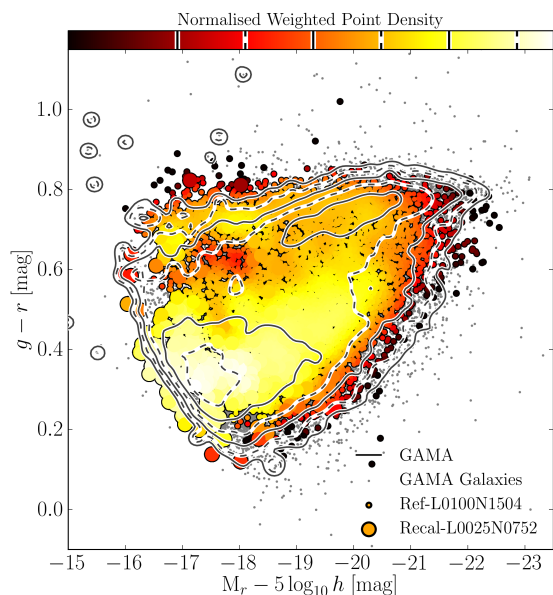


Figure 4. Rest-frame $g-r$ colour as a function of r -band absolute magnitude for EAGLE galaxies (colours) compared to a volume-limited sample of GAMA galaxies (Taylor et al. 2014, contour lines). contours and point shading is the same as in Fig 2. EAGLE photometry is obtained using the GD+O model. A composite EAGLE galaxy population is used, consisting of galaxies from Ref-100 at $M_\star > 10^9 M_\odot$ and Recal-25 at $M_\star < 10^9 M_\odot$ as in the right panel of Fig 2. There is excellent agreement between EAGLE and GAMA in the location and slope of the red-sequence ($g-r \approx 0.7$ at $M_r - 5 \log_{10} h = -20$), the appearance of a blue cloud of galaxies with $g-r \sim 0.45$ at that magnitude, which becomes increasingly blue ($g-r \sim 0.3$) for the fainter galaxies with $M_r - 5 \log h \sim -17.5$.

relatively realistic population of galaxies at low redshift, and that the modelling of emission and dust obscuration in model GD+O works well.

5 DISCUSSION

The EAGLE simulations were calibrated to reproduce the local GSMF and galaxy sizes by appropriate choice of the parameters in the subgrid model for feedback. As stellar mass is closely linked to NIR luminosity, the consistency of GSMF proxies such as the K -band luminosity function shown in Fig. 3 is not surprising, at least at $z \sim 0$. However, consistency with the luminosity functions in other broad band filters is not automatic because stellar mass, star formation history, metallicity and dust obscuration all play a role.

In Section 4, we focused on our GD and GD+O photometric models where dust absorption is approximated by a simple two component screen, with optical depths that vary with galactic gas content, metallicity and orientation (GD+O only). The colour distributions as a function of stellar mass and r -band magnitude for model GD+O in Figs. 1, 2 and 4 show a level of agreement between simulated galaxies and observations that appears unprecedented for hydrodynamical simulations, and comparable to that achieved for semi-analytical models (e.g. González et al. 2009; Henriques et al. 2014). The EAGLE luminosity functions also agree well

with observations over a range in wavelengths from optical to NIR (Fig. 3). The relatively good agreement for number density, luminosity and colour, suggests that in EAGLE each dark matter halo forms a galaxy with stellar mass, age and metallicity close to those inferred from observation. The similar level of agreement in observed colour-magnitude space also rules out a potential circularity resulting from using the same photometric model to infer stellar mass from observational data as is used in the simulations. Even though the overall level of agreement is good between EAGLE and the data, there are discrepancies.

There is an excess of bright ($M_r - 5 \log_{10} h \lesssim -20$) blue ($g-r \lesssim 0.6$) EAGLE galaxies relative to data, apparent in e.g. Fig. 4. Such an excess is seen in all our photometric models (see Fig. 1), but is least apparent for model GD+O where the recent star formation, that is the root cause of the blue colours, is most strongly obscured by dust. This parallels the findings of S15, that the fraction of passive EAGLE galaxies is too low at the high-mass end, relative to observations. It may be that massive EAGLE galaxies are too highly star forming, perhaps as a consequence of insufficient suppression of star formation by AGN. Whether the good agreement in the colour of the blue cloud, despite the underestimate of the median star formation rates at these masses (S15), suggests underestimated reddening is discussed further below.

The EAGLE red sequence, at $g-r \sim 0.75$, is flatter than observed, both when plotted as a function of stellar mass (Fig. 2) and when plotted as a function of absolute magnitude (Fig. 4). The flatter slope may be attributable to the dependence of stellar metallicity on galaxy mass, $Z_\star(M_\star)$; although stellar metallicities of EAGLE galaxies agree well with the data at the massive end, they fall less rapidly with decreasing stellar mass compared to the observational data of Gallazzi et al. (2005), as shown in S15. Numerical resolution may play a role here, because the $Z_\star(M_\star)$ of the higher-resolution simulation Recal-25 does agree with the data; see S15.

There is an abundant population of red ($g-r \sim 0.7$), low-mass ($M_\star \sim 10^9 M_\odot$) galaxies in simulation Ref-100 that is not observed (see Fig. 2a). The comparison of simulations Ref-25 and Recal-25 in Appendix B shows that this is at least partially due to a lack of numerical resolution. Indeed, star formation and outflows driven by feedback in these galaxies are poorly resolved and poorly sampled, leading to too low values of the specific star formation rate (and correspondingly too high passive fractions) and too high metallicities (see S15). Appendix A discusses the re-sampling technique we use in all models to try to mitigate poor sampling. Although this goes some way towards improving the modelling, it does not eliminate the discrepancy. Because the re-sampling is a post-processing step, it cannot help with the poor sampling of stellar feedback in these low-mass systems within the simulation. Related resolution problems are more intractable, and higher-resolution simulations are required to alleviate them.

Comparing simulations Ref-100 and Ref-25 that have identical numerical resolution (and the associated poor sampling of star formation in $M_\star \sim 10^9 M_\odot$ galaxies), yet differ in simulated volume size, allows us to isolate the effects of environment (see Appendix B). Although on average the colours of galaxies agree well between these simulations, the presence of faint red galaxies is much more pronounced in

the larger volume. This is because many of these galaxies are satellites of more massive systems that are absent in the smaller volume. The fraction of satellites increases at lower stellar masses, and in the range $10^{8.7}M_{\odot} < M_{\star} < 10^9M_{\odot}$ comprises $\sim 46\%$ of the galaxy population in the Ref-100 simulation and $\sim 33\%$ in Ref-25. Evidently, satellites contribute significantly to the colour distribution at low masses. At present we cannot verify whether improved resolution will also reduce the suppression of star formation in, or decrease the metallicities of, small satellite galaxies, which would improve the colours of $M_{\star} \sim 10^9M_{\odot}$ galaxies compared to data. We conclude that the redder colours of low-mass galaxies in EAGLE relative to data is at least partially a result of resolution, stemming from poor sampling of star formation and feedback. The improved agreement with the data that comes about from using a composite sample of Recal-25 and Ref-100 galaxies relative to using the Ref-100 sample alone is thus mainly due to improved numerical resolution, but also to the exclusion of red satellite galaxies that are not present in the smaller volume.

The level of agreement between EAGLE colours and the data also depends on the realism of our dust reddening model. Fig. 1 illustrates how dust reddening depends on the assumptions made in models N (no reddening) to model GD+O (gas metallicity, gas mass, and orientation-dependent reddening). Differences between these models are typically of order $\Delta(g-r) \sim 0.1$. A dust model that is independent of galaxy properties (such as GI) incorrectly reddens red galaxies. A reddening model that takes into account the gas mass (GD) resolves this inconsistency, with most of the remaining effects of reddening affecting blue bright galaxies. Overall, we find that the details of the dust treatments make relatively little difference to galaxy colours so that differences with observations are more likely due to the ages and metallicities of the stars rather than dust obscuration. This may be due to the relatively small effect of dust at redshifts $z \sim 0.1$. We leave the investigation of evolution of colours and luminosities in EAGLE to a future work.

Taken at face value, the specific star formation rates of star-forming galaxies in EAGLE are lower than inferred from observations by ~ 0.2 dex (S15). The fact that the colours of those same galaxies nevertheless agree with the data might imply that we underestimate dust reddening. Indeed, an underestimate of the gas fraction would lead to both an underestimate of the specific star formation rate and, at fixed metallicity, the attenuation. Lagos et al. (2015) have shown that at $M_{\star} \sim 10^{10}M_{\odot}$ the median H_2 fraction in EAGLE is about 0.2 dex lower than observed, and that this discrepancy goes away at higher masses and for the higher-resolution Recal-25 model.

Systematically lower attenuation for faint galaxies could thus be attributable to their low gas masses in the simulations. However, more complex models yield non-zero levels of attenuation even for very low gas surface densities (e.g. Boquien et al. 2013). The realism of mixed screen models as used here has been shown to break down when screens are optically thick (e.g. Disney et al. 1989). As dust optical depths are expected to be higher in blue bands, our dust prescription may be too crude to reproduce the data at higher levels of obscuration. This could contribute to the bluer colours of massive galaxies in EAGLE.

However, it is also possible that the levels of obscura-

tion *are* realistic, but that star formation rates are overestimated in the data due to the absolute calibration of observed tracers of star formation. The calibration of star formation rates from tracers rely on assumptions about the intrinsic UV continuum (from population synthesis modelling) and absorption at short wavelengths, as well as an assumed form for the IMF (e.g. Kennicutt 1998). The cumulative build-up of stellar mass in EAGLE is lower than observed by about 0.1 dex, whereas the star formation rate is lower than that observed by 0.2-0.4 dex, depending on redshift (Furlong et al. 2014). This slight tension may suggest a small overestimate of the observationally inferred star formation rates. Estimating intrinsic properties from observables of simulated galaxies (such as star formation rates) may help to clarify these issues, see e.g. the recent study by Torrey et al. (2014).

The dust model we developed here was designed to be as simple as possible, yet to avoid unrealistic levels of reddening. The model assigns a single value of reddening per galaxy without taking into account the non-uniform distributions of dust apart from that assigned to birth clouds. It is possible to make much more detailed estimates of reddening using 3D radiative transfer (RT) calculations (e.g. Baes et al. 2005; Jonsson et al. 2009). We postpone comparisons of the current simple model to those obtained with the radiative transfer code SKIRT (Baes et al. 2005) to future work.

6 SUMMARY & CONCLUSIONS

We have calculated broad band luminosities of simulated galaxies taken from the EAGLE (Evolution and Assembly of GaLaxies and their Environments) suite of hydrodynamic simulations (S15, Crain et al. 2015), and compared them to observations of the redshift $z \sim 0.1$ galaxy population. The model uses simple stellar population modelling based on the GALAXEV population synthesis models of Bruzual & Charlot (2003). To reduce sampling noise arising from single young star particle in poorly resolved galaxies, we use the re-sampling procedure described in Appendix A. In all models, galaxy luminosities are found by summing the particle luminosities within a 30 pkpc radius spherical aperture for consistency with previous analysis (S15, Furlong et al. 2014), which has been shown to mimic Petrosian apertures. Absolute magnitudes are presented in the AB system.

We compare and contrast three models of dust obscuration and to model N which neglects dust. Model GI, inspired by Charlot & Fall (2000), includes contributions to the dust optical depth from the birth clouds of young stars and from a constant dust screen, with parameters that are independent of the galaxy properties. Applying a single diffuse dust correction to all galaxies incorrectly reddens ellipticals and we avoid this with model GD in which dust reddening depends on gas phase metallicity as well as gas mass. Finally, model GD+O uses a simple geometric model to account for orientation effects, which are however small.

These simple models allow us to investigate the dependence of galaxy colours on stellar metallicities and ages, gas metallicities, and dust obscuration. Our main conclusions are as follows:

- The GI dust prescription which applies a reddening that is independent of galaxy properties, and was used by e.g. Torrey et al. (2014), excessively reddens the red-sequence

population of galaxies. As a consequence, $g - r$ colours of massive ($M_\star \gtrsim 10^{10.5} M_\odot$) EAGLE galaxies are ~ 0.1 mag redder than observed, in spite of having ages and stellar metallicities that are similar to those inferred (Fig 1b). Scaling dust optical depths with cold gas mass and gas metallicity, as in model GD, is more realistic and improves agreement with observation (Fig 1c and 1d).

- The red sequence in EAGLE is ~ 0.1 mag bluer in $g - r$ than observed for $M_\star \gtrsim 10^{11.2} M_\odot$, and has a shallower dependence on stellar mass than observed (Fig. 1). This is most likely a consequence of the dependence of colour on stellar metallicities.

- The appearance of a faint red sequence in the Ref-100 simulation run ($M_\star < 10^{9.75} M_\odot$, $0.6 < g - r < 0.8$, see left panel of Fig 2) that is not observed, is largely an effect of numerical resolution. Star formation and outflows are not well resolved in galaxies of such low mass.

- A ‘blue cloud’ of star forming galaxies appears in EAGLE below $M_\star \lesssim 10^{10.5} M_\odot$, with $g - r$ colour in agreement with the GAMA data from Taylor et al. (2014) (left panel of Fig 2).

- There is an excess of bright ($M_r - 5 \log_{10} h \lesssim -20$) blue ($g - r \lesssim 0.6$) galaxies in EAGLE relative to the data. This may be caused by an underestimate of the reddening in star forming regions, or an overestimate of the star formation rates in these massive galaxies due to insufficient suppression of star formation by AGN.

- The $z = 0.1$ galaxies taken from EAGLE transition from mostly red ($g - r \sim 0.7$) above $M_\star \sim 10^{10.5} M_\odot$ to mostly blue (ranging from $g - r \sim 0.5$ at $M_\star \sim 10^{10.5} M_\odot$ becoming bluer with decreasing mass to $g - r \sim 0.35$ at $M_\star \sim 10^9 M_\odot$) at lower masses, follows the colours of GAMA galaxies from Taylor et al. (2014) (see Fig.2). However the blue cloud persists to higher than observed stellar masses, consistent with a similar trend in passive fractions shown in S15.

- The $z = 0.1$ galaxy luminosity functions constructed from the EAGLE population agree well with data from UV to NIR bands, with differences of the order of the difference between using Kron and Petrosian magnitudes in the data (Fig. 3). This level of agreement is similar to the agreement between the EAGLE and observed stellar mass functions. In particular, there is a slight underestimate in the number density of galaxies close to the knee of the Schechter fit, and the faint-end tends to be slightly steeper than observed in most bands. We note, however, that the faint-end of the luminosity function is uncertain, especially in NIR bands, and single Schechter fits tend to underestimate the faint-end slope (Loveday 1998). Good agreement was not surprising in the NIR where luminosities are dominated by stellar mass, whereas the good agreement in other bands suggests that the star formation histories and metal enrichment in EAGLE galaxies are relatively realistic.

- The $z = 0.1$ $g - r$ colour versus M_r magnitude diagram for galaxies with $M_\star \gtrsim 10^9 M_\odot$ yields a level of agreement with data that is comparable to that of current semi-analytic models (Fig. 4; González et al. 2009; Henriques et al. 2014). The similar colour distributions of N and GD+O photometries (Fig. 1d) suggests that the dust model plays only a minor role in this agreement. This further attests to the relatively realistic evolution of the EAGLE galaxy population.

The general agreement in the colour and luminosity of EAGLE galaxies and observed galaxies suggests that the sim-

ulated galaxies have similar star formation histories, metal enrichment processes, and current star formation rates as observed galaxies. This makes the EAGLE suite well-suited to investigate the physical processes that shape galaxies through cosmic time.

ACKNOWLEDGEMENTS

The authors would like to extend gratitude to Ned Taylor and John Loveday for the kind provision of observational datasets for comparison in this work. The authors would also like to thank Alessandro Bressan, Stéphane Charlot and Claudia Maraston for their invaluable insight into the calibration and application of stellar population models. The authors also thank the GAMA Team for the use of GAMA survey data products in advance of its public release from the GAMA website <http://www.gama-survey.org/>. This work was supported by the Science and Technology Facilities Council [grant number ST/F001166/1], by the Interuniversity Attraction Poles Programme initiated by the Belgian Science Policy Office ([AP P7/08 CHARM], by ERC grant agreement 278594 - GasAroundGalaxies, and used the DiRAC Data Centric system at Durham University, operated by the Institute for Computational Cosmology on behalf of the STFC DiRAC HPC Facility (www.dirac.ac.uk). This equipment was funded by BIS National E-infrastructure capital grant ST/K00042X/1, STFC capital grant ST/H008519/1, and STFC DiRAC Operations grant ST/K003267/1 and Durham University. DiRAC is part of the National E-Infrastructure. RAC is a Royal Society University Research Fellow. The data used in the work is available through collaboration with the authors.

REFERENCES

- Allende Prieto C., Lambert D. L., Asplund M., 2001, *ApJ*, 556, L63
- Asplund M., Grevesse N., Sauval A. J., Allende Prieto C., Kiselman D., 2004, *A&A*, 417, 751
- Baes M., Dejonghe H., Davies J. I., 2005, in *American Institute of Physics Conference Series*, Vol. 761, *The Spectral Energy Distributions of Gas-Rich Galaxies: Confronting Models with Data*, Popescu C. C., Tuffs R. J., eds., pp. 27–38
- Baldry I. K., Alpaslan M., Bauer A. E., et al., 2014, *MNRAS*, 441, 2440
- Baldry I. K., Glazebrook K., Brinkmann J., et al., 2004, *ApJ*, 600, 681
- Baldry I. K., Robotham A. S. G., Hill D. T., et al., 2010, *MNRAS*, 404, 86
- Bell R., Rodgers A., 1969, *Monthly Notices of the Royal Astronomical Society*, 142, 161
- Benson A. J., Bower R. G., Frenk C. S., et al., 2003, *ApJ*, 599, 38
- Bernardi M., Meert A., Sheth R. K., et al., 2013, *MNRAS*, 436, 697
- Booth C. M., Schaye J., 2009, *MNRAS*, 398, 53
- Boquien M., Boselli A., Buat V., et al., 2013, *A&A*, 554, A14

- Bower R. G., Benson A. J., Malbon R., et al., 2006, *MNRAS*, 370, 645
- Bressan A., Fagotto F., Bertelli G., Chiosi C., 1993, *A&AS*, 100, 647
- Bruzual G., Charlot S., 2003, *Monthly Notices of the Royal Astronomical Society*, 344, 1000
- Chabrier G., 2003, *PASP*, 115, 763
- Charlot S., Fall S. M., 2000, *ApJ*, 539, 718
- Cole S., Lacey C. G., Baugh C. M., Frenk C. S., 2000, *MNRAS*, 319, 168
- Conroy C., Gunn J. E., White M., 2009, *ApJ*, 699, 486
- Crain R. A., Schaye J., Bower R. G., et al., 2015, *ArXiv e-prints*, astro-ph/1501.01311
- Crain R. A., Theuns T., Dalla Vecchia C., et al., 2009, *MNRAS*, 399, 1773
- Creasey P., Theuns T., Bower R. G., 2013, *MNRAS*, 429, 1922
- , 2015, *MNRAS*, 446, 2125
- Croton D. J., Springel V., White S. D. M., et al., 2006, *MNRAS*, 365, 11
- Cullen L., Dehnen W., 2010, *MNRAS*, 408, 669
- da Cunha E., Charlot S., Elbaz D., 2008, *MNRAS*, 388, 1595
- Dalla Vecchia C., Schaye J., 2012, *MNRAS*, 426, 140
- Davis M., Efstathiou G., Frenk C. S., White S. D. M., 1985, *ApJ*, 292, 371
- Dekel A., Silk J., 1986, *ApJ*, 303, 39
- Disney M., Davies J., Phillipps S., 1989, *MNRAS*, 239, 939
- Doi M., Tanaka M., Fukugita M., et al., 2010, *AJ*, 139, 1628
- Dolag K., Borgani S., Murante G., Springel V., 2009, *MNRAS*, 399, 497
- Driver S. P. *et al.*, 2012, *MNRAS*, 427, 3244
- Driver S. P., Hill D. T., Kelvin L. S., et al., 2011, *MNRAS*, 413, 971
- Driver S. P., Norberg P., Baldry I. K., et al., 2009, *Astronomy and Geophysics*, 50, 12
- Durier F., Dalla Vecchia C., 2012, *MNRAS*, 419, 465
- Efstathiou G., 1992, *MNRAS*, 256, 43P
- Fischera J., Dopita M. A., Sutherland R. S., 2003, *ApJ*, 599, L21
- Furlong M., Bower R. G., Theuns T., et al., 2014, *ArXiv e-prints*, astro-ph/1410.3485
- Gallazzi A., Charlot S., Brinchmann J., White S. D. M., Tremonti C. A., 2005, *MNRAS*, 362, 41
- Genel S., Vogelsberger M., Springel V., et al., 2014, *MNRAS*, 445, 175
- González J. E., Lacey C. G., Baugh C. M., Frenk C. S., Benson A. J., 2009, *MNRAS*, 397, 1254
- Gonzalez-Perez V., Lacey C., Baugh C., et al., 2014, *Monthly Notices of the Royal Astronomical Society*, 439, 264
- Gonzalez-Perez V., Lacey C. G., Baugh C. M., et al., 2014, *MNRAS*, 439, 264
- Grootes M. W., Tuffs R. J., Popescu C. C., et al., 2013, *ApJ*, 766, 59
- Haardt F., Madau P., 2001, in *Clusters of Galaxies and the High Redshift Universe Observed in X-rays*, Neumann D. M., Tran J. T. V., eds.
- Henriques B., White S., Thomas P., et al., 2014, *ArXiv e-prints*, astro-ph/1410.0365
- Henriques B. M. B., White S. D. M., Thomas P. A., et al., 2013, *MNRAS*, 431, 3373
- Hewett P. C., Warren S. J., Leggett S. K., Hodgkin S. T., 2006, *MNRAS*, 367, 454
- Hill D. T., Kelvin L. S., Driver S. P., et al., 2011, *MNRAS*, 412, 765
- Hopkins P. F., 2013, *MNRAS*, 428, 2840
- Hopkins P. F., Quataert E., Murray N., 2011, *MNRAS*, 417, 950
- Inoue A. K., 2012, *ArXiv e-prints*, astro-ph/1202.2932
- Jackson N., Bryan S. E., Mao S., Li C., 2010, *MNRAS*, 403, 826
- Jones D. H., Peterson B. A., Colless M., Saunders W., 2006, *MNRAS*, 369, 25
- Jonsson P., Groves B., Cox T. J., 2009, *ArXiv e-prints*, astro-ph/0906.2156
- Kennicutt Jr. R. C., 1998, *ARA&A*, 36, 189
- Kewley L. J., Ellison S. L., 2008, *ApJ*, 681, 1183
- Lacey C., Cole S., 1994, *MNRAS*, 271, 676
- Lagos C. d. P., Crain R. A., Schaye J., et al., 2015, *ArXiv e-prints*, astro-ph/1503.04807
- Larson R. B., 1974, *MNRAS*, 169, 229
- Lawrence A. *et al.*, 2007, *MNRAS*, 379, 1599
- Leitherer C., Schaerer D., Goldader J. D., et al., 1999, *ApJS*, 123, 3
- Loveday J., 1998, *ArXiv Astrophysics e-prints*, astro-ph/9805255
- Loveday J., Norberg P., Baldry I. K., et al., 2012, *MNRAS*, 420, 1239
- Maraston C., 2005, *Monthly Notices of the Royal Astronomical Society*, 362, 799
- Martizzi D., Faucher-Giguère C.-A., Quataert E., 2014, *ArXiv e-prints*, astro-ph/1409.4425
- McMillan P. J., 2011, *MNRAS*, 414, 2446
- Mo H., van den Bosch F., White S., 2010, *Galaxy Formation and Evolution*, *Galaxy Formation and Evolution*. Cambridge University Press
- Okamoto T., Gao L., Theuns T., 2008, *MNRAS*, 390, 920
- Oke J. B., 1974, *ApJS*, 27, 21
- Oppenheimer B. D., Davé R., Kereš D., et al., 2010, *MNRAS*, 406, 2325
- Planck Collaboration, Ade P. A. R., Aghanim N., et al., 2014, *A&A*, 571, A16
- Porter L. A., Somerville R. S., Primack J. R., Johansson P. H., 2014, *MNRAS*, 444, 942
- Price D. J., 2008, *Journal of Computational Physics*, 227, 10040
- Puchwein E., Springel V., 2013, *MNRAS*, 428, 2966
- Rahmati A., Schaye J., Bower R. G., et al., 2015, *ArXiv e-prints*, astro-ph/1503.05553
- Rees M. J., 1986, *MNRAS*, 218, 25P
- Rees M. J., Ostriker J. P., 1977, *MNRAS*, 179, 541
- Relaño M., Kennicutt Jr. R. C., 2009, *ApJ*, 699, 1125
- Robotham A., Driver S. P., Norberg P., et al., 2010, *PASA*, 27, 76
- Rosas-Guevara Y. M., Bower R. G., Schaye J., et al., 2013, *ArXiv e-prints*, astro-ph/1312.0598
- Rosdahl J., Schaye J., Teyssier R., Agertz O., 2015, *ArXiv e-prints*, astro-ph/1501.04632
- Sawala T., Frenk C. S., Fattahi A., et al., 2014, *ArXiv e-prints*, astro-ph/1406.6362
- Schaye J., 2004, *ApJ*, 609, 667
- Schaye J., Crain R. A., Bower R. G., et al., 2015, *MNRAS*, 446, 521

- Schaye J., Dalla Vecchia C., 2008, MNRAS, 383, 1210
- Schaye J., Dalla Vecchia C., Booth C. M., et al., 2010, MNRAS, 402, 1536
- Schechter P., 1976, ApJ, 203, 297
- Shen S., Mo H. J., White S. D. M., et al., 2003, MNRAS, 343, 978
- Sivanandam S., Graham J. R., Abraham R., et al., 2012, in Society of Photo-Optical Instrumentation Engineers (SPIE) Conference Series, Vol. 8446, Society of Photo-Optical Instrumentation Engineers (SPIE) Conference Series, p. 43
- Springel V., 2005, MNRAS, 364, 1105
- Springel V., White S. D. M., Tormen G., Kauffmann G., 2001, MNRAS, 328, 726
- Stancifffe R. J., Jeffery C. S., 2007, MNRAS, 375, 1280
- Taylor E. N., Hopkins A. M., Baldry I. K., et al., 2014, ArXiv e-prints, astro-ph/1408.5984
- Thoul A. A., Weinberg D. H., 1995, ApJ, 442, 480
- Tokunaga A. T., Vacca W. D., 2005, PASP, 117, 1459
- Torrey P., Snyder G. F., Vogelsberger M., et al., 2014, ArXiv e-prints, astro-ph/1411.3717
- Tremonti C. A., Heckman T. M., Kauffmann G., et al., 2004, ApJ, 613, 898
- Tully R. B., Fisher J. R., 1977, A&A, 54, 661
- Vogelsberger M., Genel S., Springel V., et al., 2014, ArXiv e-prints, astro-ph/1405.2921
- Walcher J., Groves B., Budavári T., Dale D., 2011, Ap&SS, 331, 1
- Wendland H., 1995, Advances Comput. Math., 4, 389
- White S. D. M., Frenk C. S., 1991, ApJ, 379, 52
- White S. D. M., Rees M. J., 1978, MNRAS, 183, 341
- Wiersma R. P. C., Schaye J., Smith B. D., 2009a, MNRAS
- Wiersma R. P. C., Schaye J., Theuns T., Dalla Vecchia C., Tornatore L., 2009b, MNRAS
- Worthey G., 1994, ApJS, 95, 107
- York D. G., Adelman J., Anderson Jr. J. E., et al., 2000, AJ, 120, 1579
- Zahid H. J., Dima G. I., Kudritzki R.-P., et al., 2014, ApJ, 791, 130
- Zaragoza-Cardiel J., Font J., Beckman J. E., et al., 2014, MNRAS, 445, 1412

APPENDIX A: RE-SAMPLING

Young stellar populations are optically much brighter and bluer than older populations, due to the presence of O, B and A type stars. As such, the convergence of optical magnitudes and colours depend on wavelength and star formation in a complex way. Coarse sampling of young star particles is expected to introduce Poisson scatter in the colour distribution of low-mass galaxies. The standard resolution particle mass of $m_g = 2 \times 10^6 M_\odot$ is ~ 2 orders of magnitude larger than individual HII regions (Zaragoza-Cardiel et al. 2014; Relaño & Kennicutt 2009), so this scatter may be artificially high in the simulations compared to observed galaxies.

To mitigate this effect, we re-sample recent star formation in the simulation outputs at finer mass resolution than the simulation gas particle mass. The re-sampling procedure assumes that the galactic star formation rate is constant over the previous 100 Myr of galaxy evolution. The general procedure is outlined below.

Gas particles with non-zero star formation rates and star particles that formed within the past 100 Myr are first identified. Star formation rates of progenitor gas particles are then obtained for the selected star particles. We calculate the star formation rates for star particles using the stored gas density at birth and initial particle masses (see Schaye 2004), and assume that the progenitor particles lie on the equation of state (see S15). We then take the sum of the star formation rates found for the gas and young stars to be the galactic star formation rate.

We then use some discretisation mass, m_{dis} , to represent the mass of re-sampled star particles. Each selected star or gas particle is split into the integer number of equal-mass subparticles yielding a subparticle mass closest to m_{dis} . We also obtain the ratio of subparticle mass over progenitor particle star formation rate and interpret this as a conversion timescale for each subparticle to become a star particle. We then randomly sample individual conversion times t for subparticles using an exponential distribution of the appropriate timescale. If $t < 100$ Myr, a subparticle is deemed to be converted into a star particle with $t_{\text{age}} = t_i$, a mass equal to the subparticle mass and the Z_* value inherited from the parent particle.

For our analysis we use $m_{\text{dis}} = 10^4 M_\odot$ as our target re-sampling mass resolution. This represents a more reasonable HII region mass, to better reproduce the discretisation in observed galaxies. To illustrate the effect of re-sampling, the left-hand panel of Figure A1 shows the $g-r$ colour and age of individual star particles in an actively star-forming EAGLE galaxy. We also plot the cumulative colour of the galaxy by star particle age as a black line. This shows the influence that the few youngest star particles can have on the colour of the entire galaxy. The left and right panels show the result with and without re-sampling respectively, yielding different overall colours for the galaxy (seen as the rightmost point of the black line). The presence of a single very young star particle in the simulation output causes this galaxy to appear ~ 0.2 mag bluer than with re-sampling. Though re-sampling can have a significant effect on individual galaxy colours, the colour distributions for the entire EAGLE population are only marginally affected. At the low-mass end, the re-sampling generally serves to tighten the $g-r$ colour distribution, move the blue peak to slightly bluer colours (~ 0.05 mag) and to suppress extremely blue outliers.

APPENDIX B: COLOUR CONVERGENCE

As simulation Recal-25 has a factor of 8 finer mass resolution than the fiducial model Ref-100, the stellar mass threshold above which galaxies are considered well resolved is pushed to lower masses. By comparing colour distributions of the Ref-100, Ref-25 and Recal-25 simulations (Table 1, S15) for galaxies within a certain mass range, we attempt to decouple the effects of simulation volume and resolution on the colours of low-mass galaxies in EAGLE. In Figure B1 we compare colour distributions for galaxies of mass $9.45 < \log(M_*/M_\odot) \leq 10.05$ and $8.7 < \log(M_*/M_\odot) \leq 9.3$ in the top and bottom panels respectively. The histograms for differing simulation volumes have different y axis ranges, with the 25 Mpc simulation axis range a factor of 64 smaller to account for the differing simulation volumes.

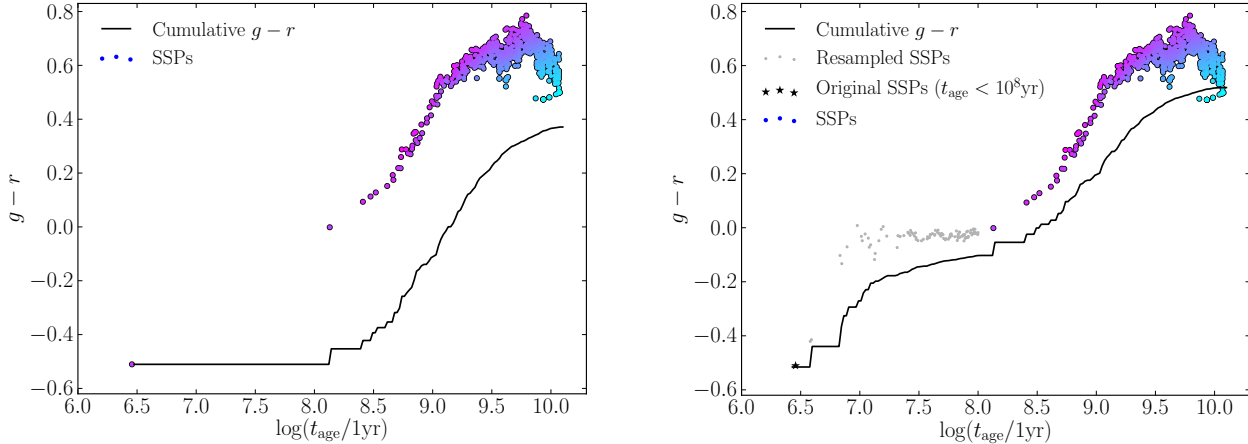


Figure A1. Demonstration of the re-sampling technique for the stellar component of an example EAGLE galaxy from the 50^3 Mpc³ box at redshift $z = 0.1$. The left panel shows particle SSP $g - r$ colours as a function of starburst age for an individual EAGLE galaxy as points coloured from blue to magenta indicating low to high metallicity. The black line indicates the cumulative galaxy colour when including particles with increasing age (from left to right) so that the far right point of the line gives the total galaxy colour. The right panel shows the same galaxy after star particles of age < 100 Myr have been re-sampled. These particles (black stars; only one in this example) are removed from the photometry calculation and the re-sampled stars (grey points) are included. This changes the cumulative $g - r$ indicated by the black line, and yields a different overall colour.

In the $9.45 < \log(M_*/M_\odot) \leq 10.05$ mass range, the position of the red and blue peaks appear roughly the same in the different simulations. However, the relative strengths of the red and blue populations differ, with the red sequence being significantly weaker than the blue cloud in the high-resolution Recal-25 model compared to Ref-100 and Recal-25. This is consistent with the lower passive fractions in the high resolution simulation at $z = 0.1$ shown in S15.

The $8.7 < \log(M_*/M_\odot) \leq 9.3$ range shows less consistency, with the red sequence becoming practically absent in the Recal-25 model while remaining in the Ref-100 and Ref-25 models. The redder colour and larger scatter of the blue population in the reference model is attributable to poor sampling of star forming gas in these galaxies. The lower star formation rates in the fiducial volume may also account for the different colours. However, we also see a larger difference between Ref-25 and Ref-100 here, particularly in the relative contributions of the red and blue populations. We attribute the higher contribution of the red sequence in the Ref-100 model to the presence of large cluster environments in the Ref-100 simulations, and thus quenched satellite galaxies, that are not sampled by the Ref-25 box. This suggests that volume effects also contribute to the weaker red sequence seen in the Recal-25 box. In both plots the greater area under the Recal-25 histogram is indicative of the systematic shift in galaxy number densities between the simulations, also seen in Figure 3.

APPENDIX C: SSP PARAMETER INFLUENCE

As intrinsic galaxy colours are sensitive to star formation histories and elemental abundance patterns, comparing EAGLE model colours directly to observed galaxy colours is a difficult way to disentangle the influence of different SSP parameters and to identify the source of any discrepancies.

To go some way towards assessing how the EAGLE stellar metallicities and star formation histories influence our mock photometry, we use the simple photometric model without dust (N). Two sets of photometric data are first generated for the simulated galaxy sample using simulation output for one parameter while using empirical relations for the other. The galaxy metallicities and light-weighted ages (LWAs) as functions of stellar mass presented by Gallazzi et al. (2005) are used to provide the empirical input. For the LWA values, we include a Gaussian scatter about the median values of the published width, which is assumed to be uncorrelated with metallicities. Clearly the assumption that galaxies may be treated as a single starburst and that the metallicity and age parameters are uncorrelated are poor, so the amount of information that can be drawn from this type analysis is limited. These plots serve as a basic qualitative illustration of the influence of different SSP parameters on galaxy colours.

The colour distributions in four M_* bins are plotted for the simulation-empirical hybrid photometry models, and are compared to the EAGLE photometry in Figure C1. The black lines indicate distributions of Ref-100 simulation galaxies. The distributions using the raw emission model with EAGLE ages and metallicities are plotted as solid histograms. The photometry models using observed LWA and Z_* values are plotted as the dashed and dotted lines, respectively. The observational data of Taylor et al. (2014) is also plotted in blue for comparison.

We see that the age parameter has the biggest influence on the colour distribution, with the empirical ages introducing a generally larger spread than metallicities, when compared to the pure EAGLE photometry. We have verified that this is still the case when we include the scatter on observed metallicity values. Figure C1 shows that giving galaxies a single age stellar population using the observational LWA data of Gallazzi et al. (2005) (dashed line) works reasonably

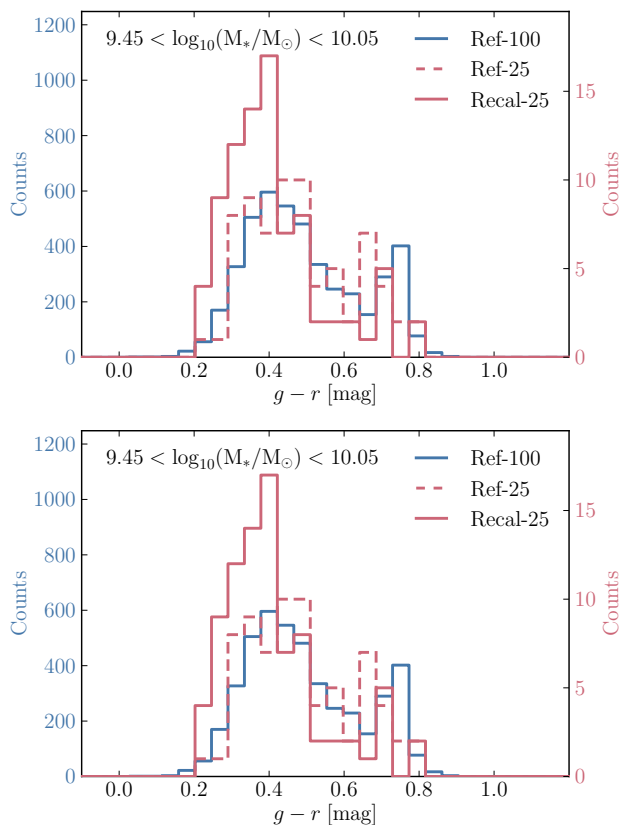


Figure B1. Comparison of $g - r$ colour distributions of the Ref-100, Ref-25 and Recal-25 simulations (see table 1) to assess the weak convergence and volume effects on model colours. Ref-100 and Ref-25 have the same resolution, while Recal-25 has a resolution 8 times finer. The top and bottom panels show galaxy stellar mass ranges of $9.45 < \log(M_*/M_\odot) \leq 10.05$ and $8.7 < \log(M_*/M_\odot) \leq 9.3$, respectively. In both panels, the blue and red histograms represent the counts per colour bin in the 100 Mpc and 25 Mpc simulations respectively. The Recal-25 and Ref-25 simulations, are plotted as solid and dashed lines, respectively. Separate y -axes are labelled and coloured to correspond to the two volumes, with their ranges scaled by a factor of 64 to account for the differing box volume. Both resolution and box size appear to significantly effect the colour distributions of low-mass EAGLE galaxies.

well in the two most massive bins where stellar populations are old. However in the lower-mass bins where galaxies are generally younger they provide a poor fit to the observed colours, inferior to our model photometry using the complex star formation histories of EAGLE (solid line).

The bimodality seen for the full EAGLE photometry in the two most massive bins, but not for in the observational LWA model, shows that the EAGLE populations are intrinsically bimodal in age. This supports the assertion that there is an excess of star forming galaxies in this regime relative to the observed population. The bluer than observed high- M_* red sequence in the observational LWA model could be a result of the lower metallicities of high- M_* galaxies. The inferior agreement of the observational LWA model relative to the full EAGLE model in the lower-mass bins suggests that the complex star formation histories of EAGLE reproduce the

data better than an empirical model assuming a single age population.

The observational Z model reveals a poor fit to observation for the two highest-mass bins. The red sequence is also much less prominent than seen in the observations and the other models across the M_* range.

The systematic effect of assuming uncorrelated scatter between the age parameter may also account for the fact that the colour distributions are broader and flatter than observed for this model, especially in the low-mass bins.

The resolution effects that drive much improved agreement between observed low-mass colours and Recal-25 relative to Ref-100 are noted in section 4 and appendix B. In the lowest-mass bin of Figure C1, we see that using observed metallicities has less impact on EAGLE colours than using observed LWAs. This indicates that star formation rate resolution is the primary resolution effect on colours, with metallicity resolution secondary to this. The presence of a faint red sequence is due to lower star formation rates and higher stellar ages than found in low-mass Ref-100 galaxies, whereas the position of the red sequence is redder by ~ 0.1 due to the higher than observed metallicities at these masses. The star formation rate resolution is also the main contributor to the redder than observed blue cloud position in Ref-100.

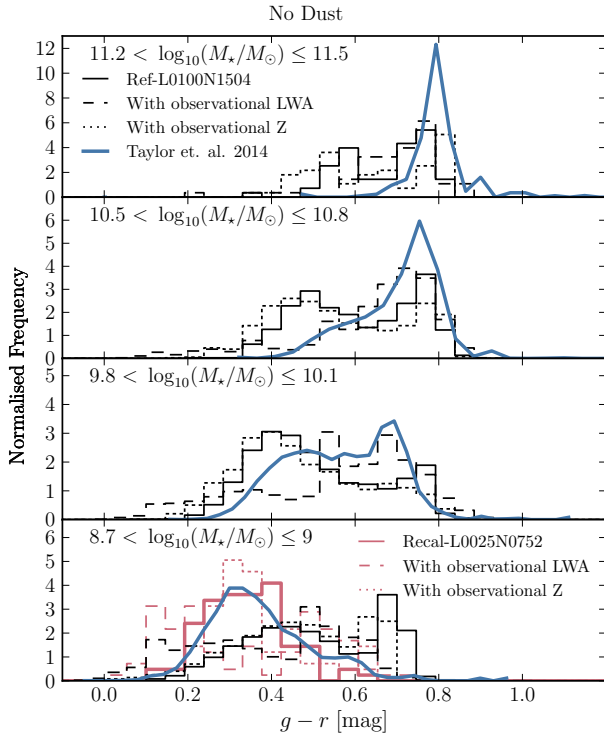


Figure C1. $g-r$ colour distributions for EAGLE galaxies for the dust-free model. The 4 panels show colour distributions for 4 bins of stellar mass, as indicated by the legend. The solid, dotted and dashed lines show the EAGLE SSP values and the EAGLE SSP values with Gallazzi et al. (2005) metallicities and ages respectively. Gallazzi metallicities and ages are assigned to each galaxy, based on the median parameter values at the galactic stellar mass. Z values are simply taken as the observed median value. The LWA values are sampled from a normal distribution with standard deviation taken from Gallazzi et. al. (2005), assuming that the scatter in age and metallicity is uncorrelated. We see that the complex star formation histories of EAGLE provide a better match to the observed colour distributions than a single SSP model using empirical values for age and metallicity.